Flagellated bacteria swimming in polymer solutions

by

Zijie Qu

B.Sc., Mechanical Engineering, Shanghai Jiao Tong University, 2013

M.Sc., Mechanical Engineering, Purdue University, 2014

A Dissertation Submitted in Partial Fulfillment of the

Requirements for the Degree of Doctor of Philosophy

in School of Engineering at Brown University

PROVIDENCE, RHODE ISLAND

May 2018

This dissertation by Zijie Qu is accepted in its present form
by School of Engineering as satisfying the
dissertation requirement for the degree of Doctor of Philosophy.

Date_____ _____

Kenneth S. Breuer, Ph.D., Advisor

Recommended to the Graduate Council

Date_____ _____

Thomas R. Powers, Ph.D., Reader

Date_____ _____

Jay X. Tang, Ph.D., Reader

Approved by the Graduate Council

Date_____ _____

Andrew G. Campbell, Dean of the Graduate School

Vitae

Zijie Qu was born on Janurary 14, 1991 in Luoyang, Henan Province, China. In 2012, he joined a combined program between Shanghai Jiao Tong University and Purdue University. Mr. Qu spent his senior year in the School of Mechanical Engineering, Purdue University as an exchange student and received his bachelor's degree from Shanghai Jiao Tong University in June 2013. Upon graduation, he spent one addition year at Purdue University and earned a Master of Science in Mechanical Engineering with a concentration in fluid mechanics. Following his graduate work at Purdue University, Mr. Qu began pursuing a Doctor of Philosophy in Engineering investigating bacteria motility in complex fluid at Brown University. Mr. Qu plans to pursue a career in academic research with an emphasis on biophysics, fluid mechanics and soft matter physics.

Preface

This dissertation consists of studies of the flagellated bacteria swimming in viscous and non-Newtonian environments and characterization of viscoelastic behavior of dilute polymer solutions using microrheology. The contents are as follows:

Chapter 1. Introduction. Included are descriptions of properties in low Reynolds number swimming problems and fundamentals of rheology.

Chapter 2. Three-dimensional real-time tracking microscopy. A description of the development on the methodology that was applied in observing and analyzing the swimming behavior of individual bacterium.

Chapter 3. "Changes in the flagellar bundling time account for variations in swimming behavior of flagellated bacteria in viscous media." *Proceedings of the National Academy of Sciences* (2018): 201714187. by Zijie Qu, Fatma Zeynep Temel, Rene Henderikx, and Kenneth S. Breuer. Experiments were conceived by Qu, Temel and Breuer, Qu and Henderikx performed the experiment and analyzed the data. The results and discussion were composed by Qu and Breuer.

Chapter 4. "Characterizing the viscoelastic behavior of dilute polymer solutions using microrheology." by Zijie Qu, Xiongfeng Yi and Kenneth S. Breuer. To be submitted. Experiments were conceived by Qu, Yi and Breuer. Preliminary experiments and analysis were done by Yi. Additional studies including data collection and analysis were completed by Qu. Results were interpreted and summarized by Qu and Breuer.

Chapter 5. "Non-Newtonian effects change flagellated bacteria motility." by

Zijie Qu and Kenneth S. Breuer. To be submitted. Experiments were conceived, executed and analyzed by Qu with Breuer providing assistance in interpretations of the results and summaries.

Chapter 6. Conclusion. Remarks and recommendations for future work.

Acknowledgements

First and foremost, I would like to thank my advisor, Dr. Kenneth S. Breuer, for giving this wonderful opportunity to me and fostering my intellectual growth throughout my time at Brown University. I appreciate all his contributions of time, ideas, and funding to make my Ph.D. experience productive and stimulating. No meaningful work could have been accomplished without his tremendous academic support. I am also thankful for the excellent example he has provided as a successful scientist and professor. In addition, I would like to thank the Ph.D. committee members, Dr. Thomas R. Powers and Dr. Jay X. Tang for their excellent teaching, kind support, and insightful comments on the work I have done at Brown University. Finally I would like to thank National Science Foundation (Chemical, Bioengineering, Environmental, and Transport Systems No. 1336638) for the financial support.

My personal thanks are due to all current and former Breuer Lab members. In particular, to Fatma Zeynep Temel who helped me significantly on my studies during the first year I spent at Brown University and to Yi Fan who constantly showed a great support on my experiment and analysis in low Reynolds number hydrodynamics throughout my Ph.D.; to Jenna Perry for offering invaluable help on culturing and storing cells; to Wencong Liu, Zekun Zhuang, Guanyang He and Wenhao Li for advice and friendship; and of course to my family.

Contents

List of Tables

List of Figures

Chapter One

Introduction

Living creatures move through their aqueous environment using various swimming strategies. Fish propel themselves by beating their caudal fins [1], jellyfish contract their body gently and create vortex ring to gain translational momentum [2]. Natural selection has ensured the mechanical systems evolved in animals are highly efficient with respect to their habitat and mode of life. Generally speaking, swimming refers to achieve a transportation in liquid by moving or deforming one's body in a certain manner. Such movement or deformation is usually cyclic as seen from most of the aquatic creatures since they keep swimming to survive.

Analyzing the mechanics of swimming creatures is important to understanding their behavior and swimming strategies and the physics of biological locomotion depends dramatically on the animal's scale. Osborne Reynolds [3] pointed out that the ratio of the inertial force to the viscous force on an object with a dimension L moving through a fluid with velocity U, is given by $\rho UL/\mu$, where ρ and μ are the density and viscosity of the fluid respectively. This ratio is called Reynolds number (Re) which is also seen in the dimensionless Navier-Stokes equation:

$$\frac{\partial \boldsymbol{u}^*}{\partial t^*} + (\boldsymbol{u}^* \cdot \nabla^*)\boldsymbol{u}^* = -\nabla^* p^* + \frac{1}{Re}\nabla^{*2}\boldsymbol{u}^*, \qquad \nabla^* \cdot \boldsymbol{u}^* = 0, \tag{1.1}$$

where * denotes the dimensionless variables and $\boldsymbol{u}^* = \boldsymbol{u}/U$, $t^* = tU/L$, $\nabla^* = L\nabla$ and $p^* = pL/\mu U$.

The Reynolds numbers of aquatic creatures span a wide range from $Re \sim 10^7$ (whale [4]) to $Re \sim 10^{-4}$ (bacteria [5]). The swimming strategies adopted by the creatures living in a low Reynolds number regime ($Re \ll 1$) are completely different from those at high Reynolds number since they have to overcome the time reversibility of Stokes flow [5, 6]. An interesting argument, proposed originally by Purcell [5] to describe such differences in swimming strategy, is widely known as the "Scallop

Theorem", and explains how reversible kinematics cannot be applied to swim at low Reynolds number. In nature, microorganisms are able to achieve transportation in low Reynolds number environment using certain swimming strategies [5, 7]. Understanding their behavior is of great scientific interests [8] and provides insights into potential engineering applications [9, 10].

In this thesis, an example of swimming at low Reynolds number will be discussed in detail - the behavior of flagellated bacteria *Escherichia coli* in both Newtonian and non-Newtonian (polymer) solutions. In addition, a microrheology experiment is performed to characterize the viscoelastic properties of the non-Newtonian polymer solutions.

1.1 Swimming at low Reynolds number

Most microorganisms swim by moving flagella attached on their cell body [11]. The flagellar filaments can be a flexible filament or a semi-rigid helix. For instance, *Chlamydomonas*, a biflagellated alga, swims by beating its flagella in a non-reciprocal manner [12]. In each stroke, the cell starts with a rigid power stroke by moving its flagella stiffly, followed by a flexible recovery stroke in which it folds its flagella closer to the cell body, and pulls them back. The difference in the viscous drag during the power and recovery strokes leads to the translational motion of the cell (Fig. 1.1). Another example of low Reynolds number swimming is provided by bacteria *E. coli* that propel themselves by rotating multiple helical filaments (Fig. 1.2). Although each filament is connected to an independent motor which is randomly distributed on the body, for the majority of the time, the cell rotates all motors in a counterclockwise direction which forms a flagellar bundle and produces a translational

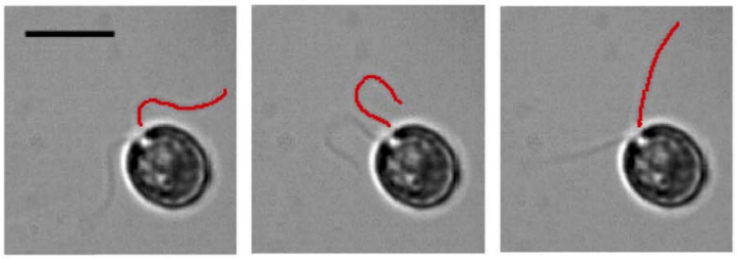

Figure 1.1: Sample snapshots of *C. reinhadtii* swimming in buffer solution; scale bar is 10 μm. Reprint from [13].

movement, called a "run". When the bacteria reverse one or more flagellar motors from counterclockwise rotation to clockwise rotation, a sudden change in orientation, called a "tumble" [8], is initiated. This "run and tumble" behavior not only allows the cell to swim at low Reynolds number regime but also provides a simple and an effective strategy for navigating through their environment, for example, to search for food [5].

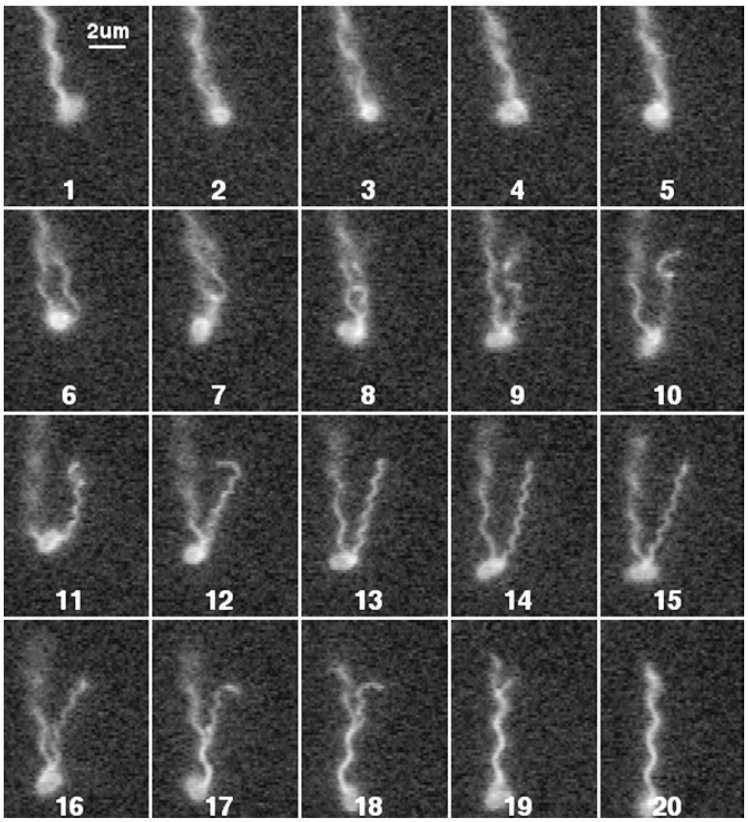

Figure 1.2: Fluorescently labeled flagella for bacteria *E.coli*. Reprint from [14].

The motility of flagellated cells has been studied extensively [15–19] and a key focus has been on how changes in the ambient environment affect the cell's swimming behavior and patterns. Many experiments [20, 21], simulations [13] and theoretical calculations [22] have been conducted on this particular problem. Some of the classical and somewhat simplified studies [5,23] suggest that an increase in viscosity leads to a decrease in cell swimming speed, however the opposite phenomenon has been observed in some of experimental works [24]. Moreover, the flagella dynamics (beating patterns, bundling dynamics) have been shown to be strongly affected by the change in viscosity or with the introduction of non-Newtonian effects [25, 26]. Since the change in flagellar locomotion usually leads to a change in swimming behavior, it is important to understand how the filamentous structures interact with each other and with the surrounding fluids.

1.2 Rheology of complex fluids

The word, "rheology", was originated from Greek meaning the study of flow. This subject is dominated by inquiry into the flow in different kinds of liquids, especially on complex fluids such as polymer solutions, suspensions, biological systems, pastes and other compounds. Complex fluids do not follow the Newton's Law of Viscosity [27], which describes the relationship between shear stress and shear rate:

$$\sigma = \mu\dot{\gamma}, \tag{1.2}$$

where σ is the shear stress, μ is the viscosity and $\dot{\gamma}$ is the shear rate. Such fluids, usually known as non-Newtonian fluids, are very commonly seen in nature and a knowledge of their behavior is essential in both industries and scientific researches.

It is important to emphasize the Newtonian behavior before concentrating on non-Newtonian effects. In the context of shear viscosity, experiments done at constant temperature and pressure with Newtonian fluid have the following characteristics. First, the shear viscosity is independent on the shear rate. Second, the viscosity has no memory, which means the shear stress falls immediately to zero when the shearing stops. Lastly, a simple shear flow generates only shear stress and normal stress differences are always zero. A fluid demonstrating any deviation from these characteristics is considered a non-Newtonian fluid.

1.2.1 Shear-thinning and shear-thickening

Viscosity is one of the most important quantities in analyzing rheological problems. Many materials, including emulsions, dispersions and polymer solutions, exhibit a shear-rate dependent viscosity. In most cases, the shear viscosity decreases with increased shear rate and such effect is called "shear-thinning". While an opposite behavior, that shear viscosity increases with increased shear rate is called "shear-thickening". The most commonly used model for such fluids is the power-law model or the Ostwald-de Waele model [28]:

$$\mu(\dot{\gamma}) = m\dot{\gamma}^{n-1}, \tag{1.3}$$

where m is called the consistency index and is related to the magnitude of the viscosity; the exponent of $\dot{\gamma}$, $n-1$, describes how strongly the viscosity depends on the shear rate. In the case of Newtonian fluid, $m = \mu$ and $n = 1$. Both m and n are usually fitted with the data from experimental measurements.

1.2.2 Viscoelastic effects

One of the most spectacular non-Newtonian effects, which differs qualitatively from the behavior of Newtonian fluids, is the viscoelastic effect. This particular phenomenon is exhibited by polymers and their mixtures. It is commonly seen and experienced in our kitchen. For example, when pure water is stirred with mixing blade in a bowl, centrifugal force drives the water to move away from the blade and towards the bowl walls. However, an opposite effect is observed while stirring a water-flour mixture, even at high stirring speed. The mixture climbs the mixing blade, a phenomenon called the Weissenberg, or rod-climbing, effect. This cannot be explained by relations that govern the Newtonian fluid but is due to a shear-induced normal force that acts on the mixture as a result of the viscoelastic nature of the material.

Another interesting behavior about viscoelastic fluid is the memory effect. Materials such as toothpaste, silly putty and dough exhibit elastic behavior on a short time scale, while on a longer timescale they flow as a liquid. When Newtonian fluids are subjected to stress, they flow, and when the stress is removed, the deformation stops immediately. Viscoelastic fluids also deform under external stress, but when the stress is removed, the stress inside the fluid does not vanish instantly and the internal structure of such fluid allows it to sustain stress for some time, which is called relaxation time. Several mathematical models including the Maxwell model [29] have been developed to describe this nonlinear behavior.

1.3 Summary and scope of this thesis

The swimming motility of microorganism is of great interest in both biophysics and biomedical applications. The mechanism of their transportation is relevant to a wide range of problems including biofilm formation [30] and biodegradation of environmental pollutants [31]. More importantly, since most of the natural living environment for microorganism are complex polymer solutions, such as mucus, it is then essential to understand how these creatures navigate through the polymer networks and to be able to model the propulsion mode at low Reynolds number in these complex media.

In this thesis, we study the motility of bacteria *E. coli* in both Newtonian (Chapter 3) and non-Newtonian (Chapter 5) polymer solutions. In addition, we also characterize the viscoelastic behavior of dilute polymer solutions (Chapter 4) used as non-Newtonian agents in our bacteria motility studies. A microrheology experiment based on standard fluorescence microscopy and Statistical Particle Tracking method was performed in analyzing the mean-square displacements (MSD) of dispersive particles in such solutions. The relaxation time and viscoelastic moduli are calculated from the MSD.

Chapter Two

The three-dimensional real-time tracking microscope

2.1 Introduction

Three-dimensional tracking microscopy has been widely used in the study of bacteria motility [32–34] and particle dynamics on a microscopic scale [35]. This technique has been evolving through the past few decades [7, 32, 36] and is becoming an invaluable tool in various scientific disciplines including fluid mechanics, microbiology, rheology etc.

Large ensemble measurements in microscopic system are useful in generating average quantities such as mean bacterial swimming speed [34, 37] and mean square displacement (MSD) of diffusing particles [38]. Many imaging techniques such as holography [37, 39] and confocal microscopy [40] are used to track micro objects in three dimensions. In these types of experiments, the positions (trajectories) of the tracked objects are post-processed from the images and the samples are generally observed upon a stationary microscope platform.

Although tracking micro objects using such techniques are effective and straightforward, the total tracking time for each object is highly limited due to the fact cells may quickly pass through the observation window and particles may diffuse out of the focal plane. Therefore, single object tracking, which extends the tracking time for each individual, is desirable to provide a better insight of the system in many aspects, for example the individual behavioral differences among a group of cells [7, 33] and interactions between passive particles [41]. For example, Berg and Brown [7] discovered the "run and tumble" nature of wild type *Escherichia coli* by tracking individual cells for a relatively long time. In general, the objective and the sample need to be physically moved in real time to achieve such long-term individual tracking [7, 33].

In this chapter, a three-dimensional real-time individual tracking microscope is applied to study cell motility and particle dynamics. Both phase contrast microscopy and fluorescence microscopy can be used as imaging methods in this technique.

2.2 System configuration

The tracking system is based on a standard inverted optical microscope (Nikon TE200). As shown in Fig. 2.1, additional components are implemented on the system to achieve the tracking function. A micro stage (Prior H107) with motors and encoders is used to move the stage and read the stage position to achieve the real-time tracking function on the plane (x-y plane) that is perpendicular to the optical axis. It is connected to a step motor controller (Galil DMC-4020) to communicate with PC. A piezo positioner (Physik Instrumente, PIFOC P-721.CDQ) is implemented beneath a 20X objective (Nikon CFI Plan Fluor 20XMI) to adjust the height of focal plane in real time to realize the tracking along the optical axis (z direction). The piezo positioner is connected to a data acquisition board (National Instrument, DAQ PCI6052e) which generates and reads voltage signals that are proportional to the height of the piezo. A camera (PCO edge 5.5 sCMOS) is used to acquire images and transfer them to PC in real time for cell position analysis. All hardware are controlled with a single program written in C++ and OpenCV library.

To achieve the three-dimensional real-time tracking, the system is designed to follow a negative feedback loop as shown in Fig. 2.2. Images are taken at a certain frame rate (e.g. 60 fps), stored on the hard disk (solid state disk) and processed in real time to find the position of the tracking object. Then a feedback signal is generated and sent to the microstage controller and the piezo actuator to adjust the

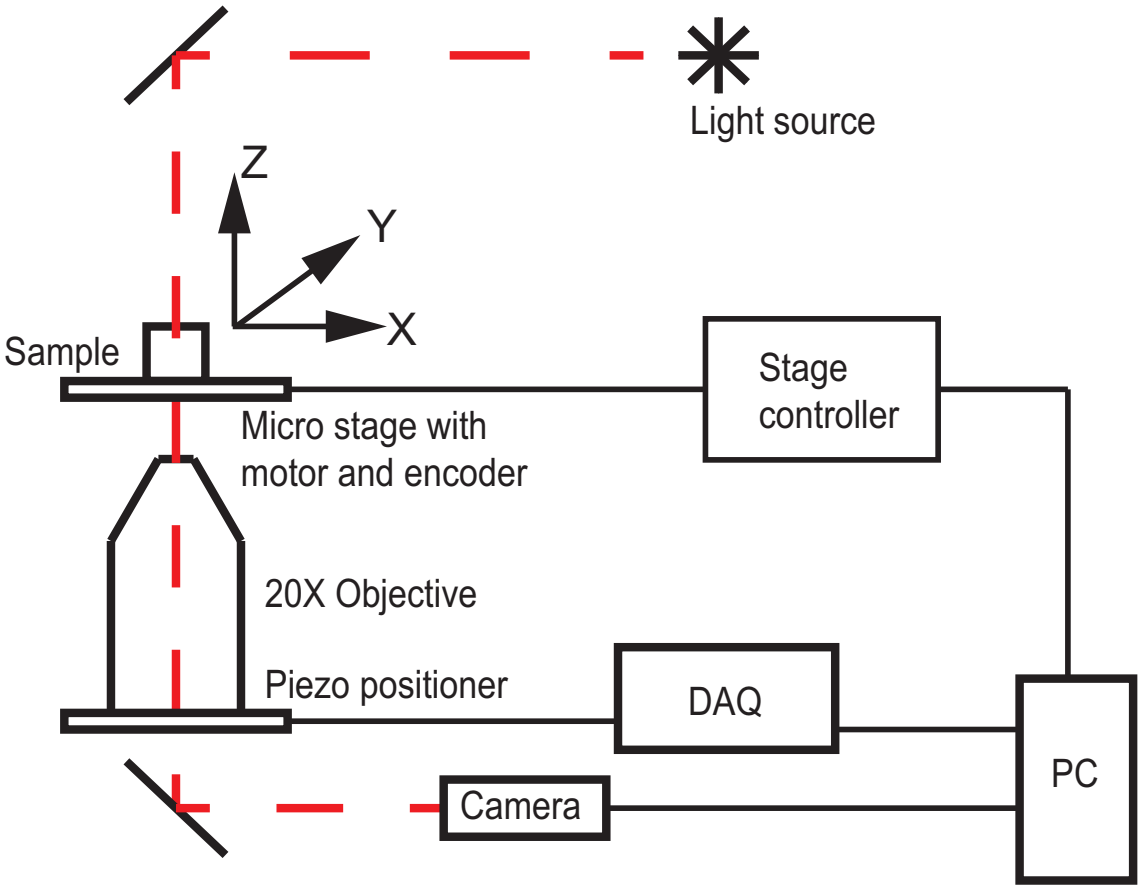

Figure 2.1: Schematic of the real-time three-dimensional tracking microscope.

position of the sample and the height of focal plane.

2.3 Methodology

2.3.1 Contour detection and tracking in x-y plane

The x, y positions of the object in the image are determined from its intensity. As shown in Fig. 2.3, the object intensity is darker compared to the background in the images taken with phase contrast microscopy (A) while brighter with fluorescence microscopy (B). The object detection in x-y plane is realized using the *threshold* and

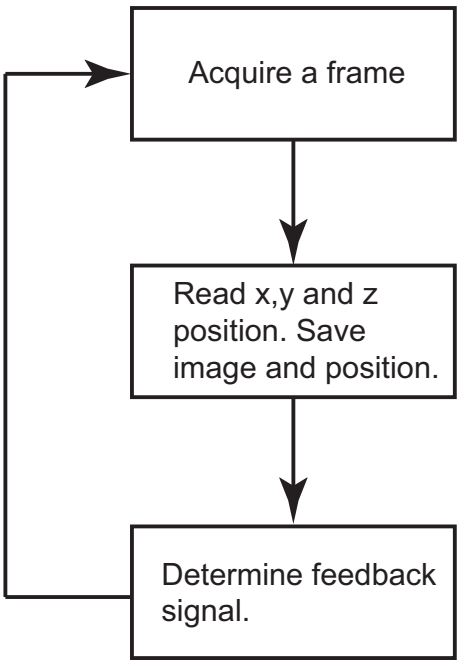

Figure 2.2: Flow chart of real-time three-dimensional tracking algorithm.

$findcoutours$ function in OpenCV library. For a given image, a binary threshold is first applied so that the normalized intensity of the objects is 1 and background is 0 [1]. Then all contours, which have an intensity of 1, are detected using $findcoutours$ function. The position of contour centroid is then calculated using *moment* function. The centroid of the object in the image is analyzed and recorded as x_p and y_p. At the beginning of each tracking event, the whole image is analyzed and a random contour is chosen to be the object tracked in this single experiment. In the following images, a small portion, which is defined as a square with 20 pixels in length centered at (x_p, y_p) instead of the whole image, is analyzed to ensure the same object is tracked throughout the experiment. Since the object position (trajectory) in the frame of reference that is fixed on the sample is interested, the x-y position of the sample, same as the position of the micro stage is read from the encoders (using TP command in Galil library) and recorded as X_s and Y_s. Linear combination of x_p, x_s and y_p, y_s gives the x and y position of the tracking object in the sample frame of reference.

[1] This is for the fluorescence microscopy, an inverted binary filter is applied on images taken with phase contrast microscopy

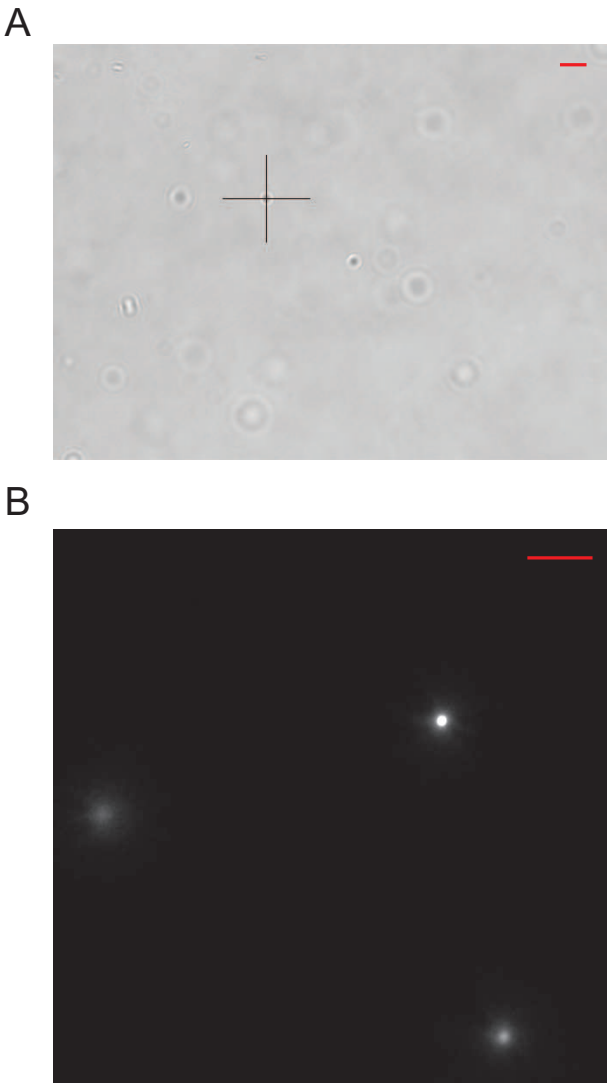

Figure 2.3: Sample images taken with phase contrast microscopy and fluorescence microscopy. Scale bar is 10 μm. A. *E.coli* cells in Ficoll solution, which are imaged using phase contrast microscopy. B. 1 μm particles diffused in water, which are imaged using fluorescence microscopy.

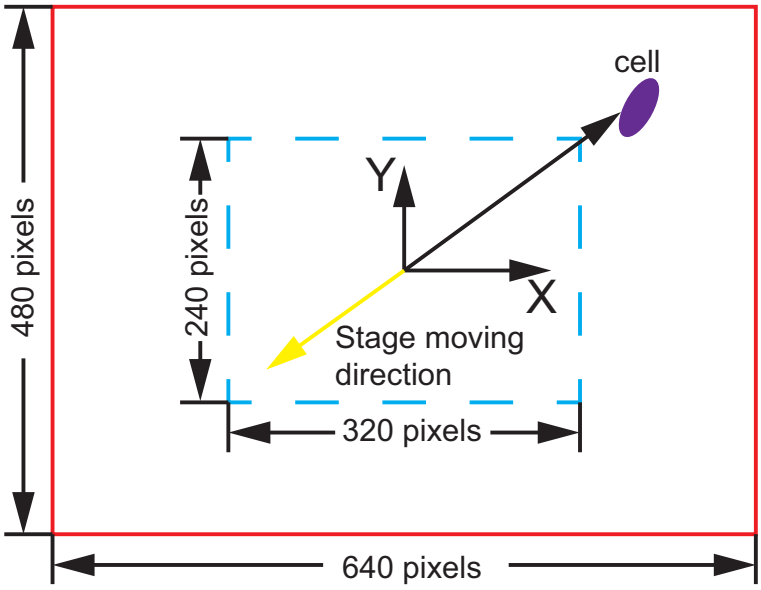

Figure 2.4: A demonstration of tracking in x-y plane.

Once the position of tracking object is measured and recorded, a feedback signal is generated to adjust the sample location. In order to move the stage as little as possible (since each movement may introduce a perturbation to the system), a virtual threshold (320×240 pixel^2) on the image is created as shown in Fig. 2.4. As soon as the centroid of the object (x_p, y_p) is detected to be out of the threshold as denoted by a dashed rectangle, the stage will move in the opposite direction just enough to bring the cell back into the threshold region. In the case shown in Fig. 2.4, the physical movement of the stage $x_{move} = x_p - 160$ and $y_{move} = y_p - 120$, where 160 and 120 are the x and y location of the threshold edge. The movement function is realized using PR and BG command from Galil library.

2.3.2 Two strategies on tracking along optical axis (z-axis)

Tracking along optical axis (z direction) depends strongly on the illumination and imaging technique. Two methodologies on tracking in z direction are given here. The

first one is with phase contrast microscopy and is typically used for tracking cells such as *E.coli*. A series of images (demonstrated in Fig. 2.5) are taken with a cell that is stuck on the coverslip surface at various objective heights (z positions). The normalized intensity (I) of the cell contour is plotted as a function of focal plane height (H) as shown in Fig. 2.6. From the result of linear fitting on the data where $H > 0$, it is noted that the normalized intensity increases linearly with respect to z location and can be described by Equation 2.1.

$$I = 0.04H + 0.47 \tag{2.1}$$

From this linear relationship, the cell's distance away from the focal plane (H) can be interpolated from its normalized intensity value (I) from each image. In experiment, the cell is set to be a bit off focus ($H = 2$ μm) which makes the tracking along optical axis possible. The intensity of the cell is measured by averaging the intensity over all pixels in the detected contour. The height of the objective (focal plane) is adjusted and monitored by a piezo positioner, which is connected to a voltage signal generator/receiver. Voltage signals are generated to drive the piezo. Feedback signals are read and recorded on PC at the same frequency as the frame rate, keeping the z position of the tracking object. Although the intensity-distance relation (Equation 2.1) is calibrated with a cell stuck on coverslip and the actual relation for a freely swimming cell in bulk region may be slightly different, the tracking still works since the displacement of the cell along z direction between consecutive images are small (~ 1 μm) and the height adjustment is fast enough to follow the swimmer.

The second tracking method along optical axis is designed for fluorescence microscopy. Although it is not used for the experiments described in the following

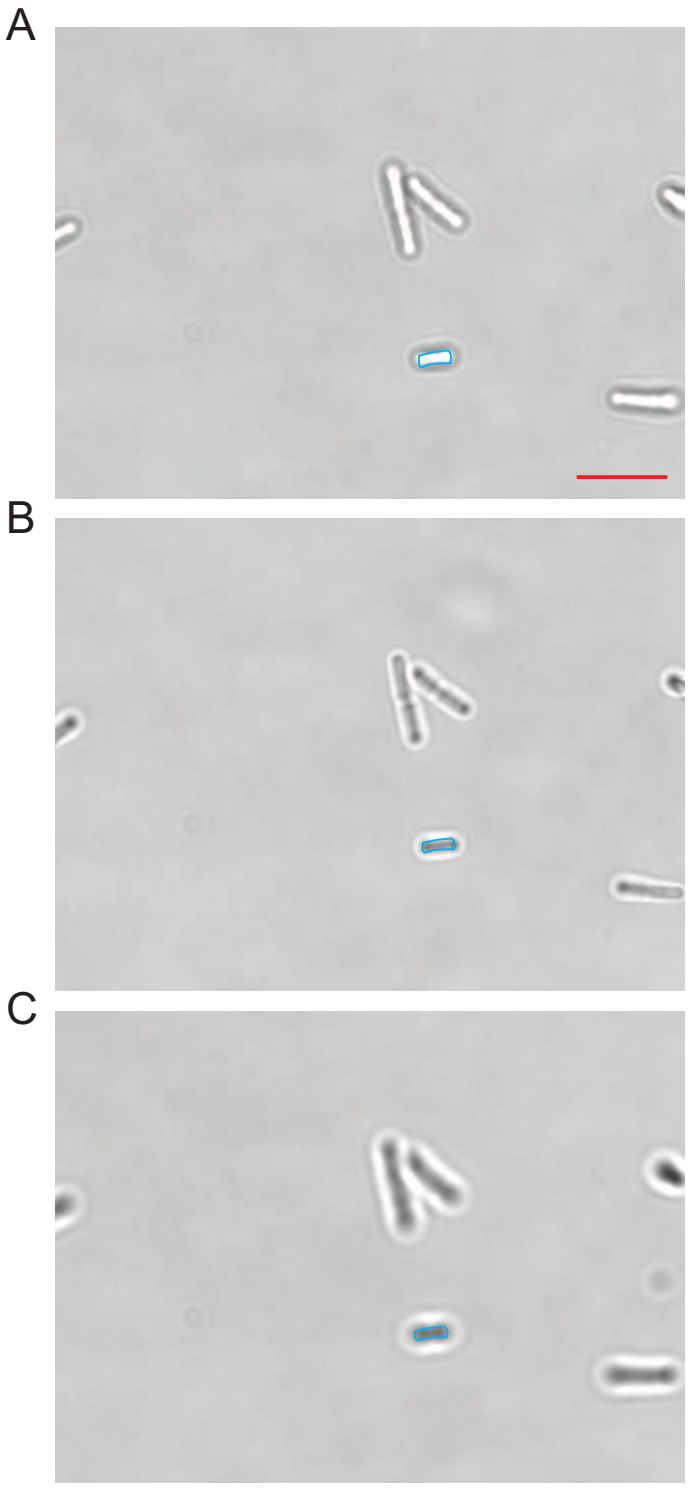

Figure 2.5: Calibration of bacteria (*E.coli*) intensity (measured in the light blue zone as detected from *contour* function) as a function of focal plane height. Cells are stuck on a coverslip and images are taken at different objective height. A. $H = 7$ μm. B. $H = 0$ μm. C. $H =$ -7 μm. Scale bar, 3 μm.

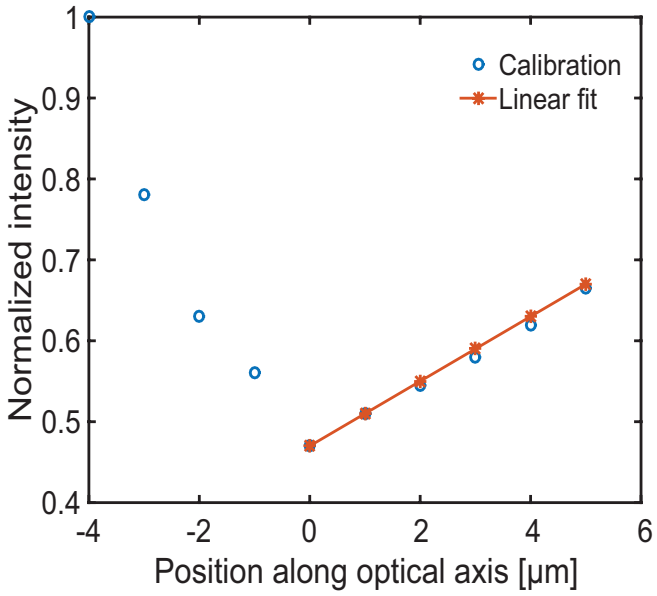

Figure 2.6: Normalized intensity of bacteria at different z positions. Images were acquired for a stuck bacteria on surface. A linear fitting is given based on data point where z >0.

chapters, three-dimensional real-time tracking with fluorescence microscopy is ideal for tracking fluorescent particles or fluorescently labeled cells. The intensity of fluorescent particles as a function of distance away from focal plane has been previously measured [36]. The idea and procedure of tracking in x-y plane is identical to the one using phase contrast microscopy. Instead of intentionally viewing the object a bit off focus, the piezo positioner is actively scanning the object at different z locations to achieve a more accurate tracking result. The scanning and image acquisition is described in Fig. 2.7. A sinusoidal wave is generated from a voltage signal generator to drive the piezo and the fluorescent particle is located in between the focal planes when the objective is at the peak and the valley of the waveform. Three images are taken consecutively when the objective is at the peak, in the middle and at the valley as shown in Fig. 2.7 position 1, 2 and 3. Since the intensity of the fluorescent particles decreases as it locates further away from the focal plane, one can easily determine whether the particle is located in the upper region (between plane 1 and 2) or the lower region (between plane 2 and 3). Once the region is measured, the

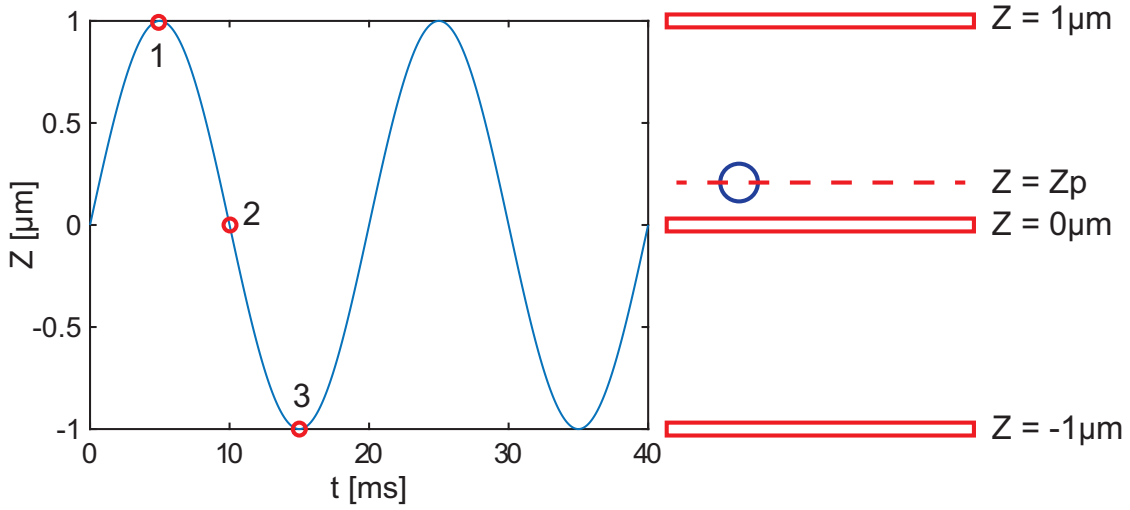

Figure 2.7: A demonstration of tracking along optical axis using active scanning. Three consecutive images are taken at location 1, 2 and 3. Intensity measurements from those three images lead to an accurate detection of particle location in z.

precise z position of the particle (z_p) is calculated using the relationship described by Levi *et al.* [36], where the intensity of the particle center (I_z) decreases to the square of the distance away from focal plan ($I_z \sim 1/(z_p - z_{focal})^2$). Then a voltage offset that moves the piezo from previous relaxing position to $z = z_p$ is added on the scanning waveform for the following tracking.

It is true that tracking with objective scanning is more accurate and the objects tracked on the image are clearer in the sense that they are closer to the focal plane. It is highly inefficient since only one image out of the three consecutive images is used for tracking reconstruction and a higher scanning frequency is necessary when the objects have a large speed along z direction. This leads to an issue when the system becomes underdamped [42] and the scanning amplitude is not guaranteed.

2.4 Summary

In this chapter, we have proposed and illustrated a three-dimensional real-time tracking microscope, which is achieved by physically moving the sample position and objective height. Two imaging techniques, phase contrast and fluorescence microscopy are used in the system to provide a wide application on various engineering and biophysics problems.

The current limitation of this tracking technique lies in the sampling frequency and working distance. A better real-time image processing strategy is crucial in raising the sampling frequency, which is necessary in tracking swimmers with a higher speed. GPU enhanced algorithm is one of the possible solution for such a limitation. The working distance, especially along optical axis, is restricted by the traveling distance of the piezo positioner. A combination of piezo driven adjustment (fast but short in distance) and motorized stage along optical axis (slow but long in distance) is probably a way to enhance the total working distance of the system, but requires a delicate controlling strategy.

Chapter Three

Changes in the flagellar bundling time account for variations in swimming behavior of flagellated bacteria in viscous media

3.1 Introduction

The survival of motile bacteria depends in part on the ability to navigate their environment, swimming towards attractants (e.g. food) and away from repellents (e.g. toxins). In order to move in a low Reynolds number environment and to avoid the time-reversibility of Stokesian dynamics [5], flagellated bacteria such as *Escherichia coli* exhibit a non-reciprocal swimming behavior first described by Berg and Brown [7]. The "run-and-tumble" behavior is characterized by extended linear movements ("runs") punctuated by sudden changes in direction ("tumbles"). The tumbling event is initiated by the clockwise (CW) rotation of one or more of the flagellar motors [8, 14] (T_o in Fig. 3.1A). This precipitates the unravelling of the flagellar bundle which causes the cell to immediately stall and re-orient ($T_o \rightarrow T_1$). As the motor returns to counter-clockwise (CCW) rotation (T_2), the flagellar bundle re-forms ($T_2 \rightarrow T_3$) [14, 26] and the cell accelerates back to its characteristic run speed, U_o. Note that the value of U_o can vary, and depends on the cell metabolism, the number, length and spatial distribution of flagella and the conditions of the surrounding fluid (presence or absence of nutrients, etc).

This mode of cell motility has been studied extensively over the past decades [23, 30, 32, 34, 43–47] and while it remains a compelling idealized model for multi-flagellated motion, there remain questions. For example, Molaei *et al.* analyzed thousands of individual cell motion histories [37] and reported that only 70% of the *E.coli* cells exhibited run-and-tumble style of motion while the rest of the cells, moved in a different mode, termed "slow-random-walk" and characterized by a slower average speed and absent clearly-defined tumbling events. More recently, a close examination of cell motility and flagellar motion [48] revealed intermediate states, such as partial unbundling, which also contributed to a wider variety of swimming

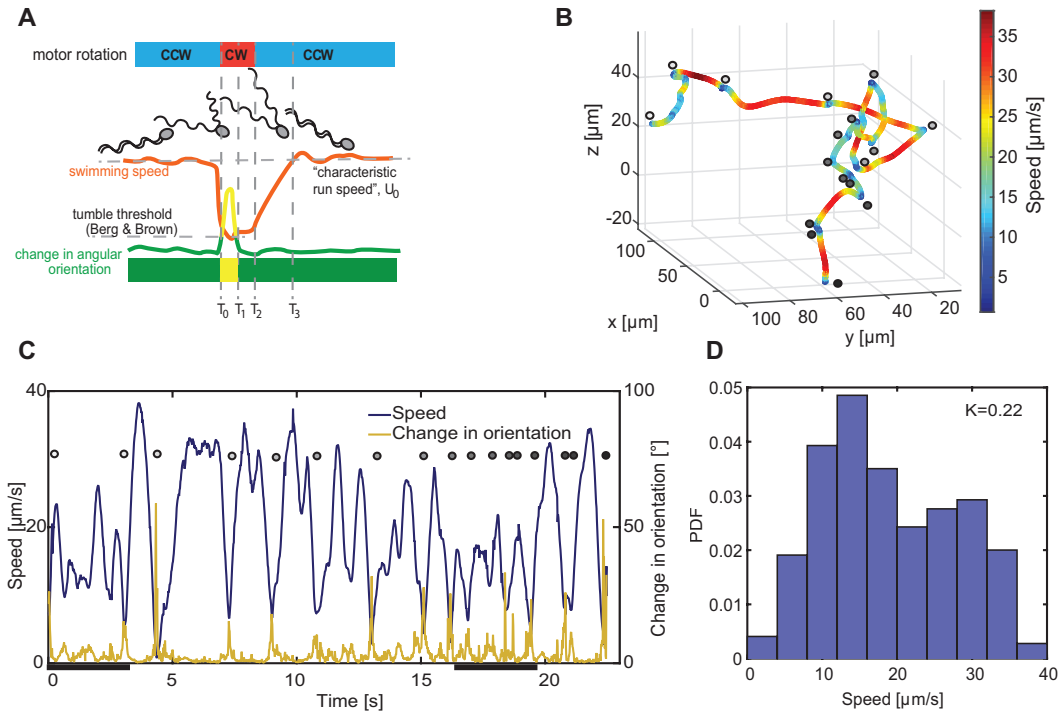

Figure 3.1: Demonstration of diverse swimming modalities. (A) Schematic of the tumbling process, (adapted from Darnton [49]). T_o: the initiation of tumble when motor starts to rotate CW; T_1: the end of tumble according to the definition given by Berg and Brown [7]; T_2: the motor starts to rotate CCW and the re-bundling is initiated; T_3: the completion of bundle process when the swimming speed reaches the characteristic run speed U_o. (B) Three-dimensional trajectory of a representative *E.coli* cell swimming in 1.25% native Ficoll 400 solution (1.17 cP); color change denotes the speed of the cell. (C) Time history of swimming speed (blue) and change in orientation (yellow); the round markers on both (B) and (C) denote a tumble event using the definition of Berg and Brown [7]. Markers with the same color refer to the same event. The black bars on the x-axis of (C) identify periods of "slow-random-walk" [37]. (D) The corresponding probability distribution function of the swimming speed; the two peaks at 12 μm/s and 30 μm/s correspond to the "slow-random-walk" and run motilities.

modalities than the binary "run" and "tumble" states.

Bacteria live in varied fluid environments that can exhibit viscous and/or viscoelastic properties [50], measurements and calculations of cell motility in these complex fluids have yielded seemingly contradictory results and explanations of swimming behavior [24, 32, 34, 51–57]. Even for cells swimming in (assumed to be) Newtonian polymer solutions of varying viscosity, the picture is unclear. One of the earliest experimental studies in polymeric solutions shows that the swimming speed is increased even when the polymer concentration is low [24]. The authors explain

this phenomenon by appealing to the properties of the loose and quasi-rigid polymer network and its interactions with the nanoscale flagellar propulsors. Magariyama and Kudo proposed a simple model based on Resistive Force Theory (RFT) [5, 58], but modified by the introduction of two apparent viscosities that depend on the length, morphology, and the interaction between polymer molecules [58]. A further complication arises from the observation that the level of biological activity appears to change with the addition of the thickening polymer [34], probably due to the metabolism of small polymer fragments by the bacteria.

In order to fully understand the different swimming modes, cells must be observed for relatively long time periods and in different fluid environments. Two methodologies are commonly described. In most studies, cells are tracked under a stationary microscope platform [34, 37] which, though effective and straightforward, only permits tracking for short times as the cells quickly pass through the microscope's field of view and focal plane. Alternatively, one can track individual cells in three dimensions by physically moving the objective and the microscope stage in real time [7, 19, 48]. Although the tracking microscope is inefficient in terms of the number of observed individuals, the extended tracking time permits detailed observation of similarities and differences in the swimming behavior for both a single cell and between individual cells in an identical genetic population.

In this experiment, in an attempt to understand the different swimming modalities and the role of viscosity on cell motility, we report on the use of tracking microscopy to measure the detailed behavior of wild-type *E.coli* swimming in Newtonian fluids of varying viscosity. Solutions of polymers using two molecular weights were prepared, and cell trajectories in both native and dialyzed polymer solutions were recorded.

3.2 Materials and methods

3.2.1 Cell preparation

The cells used in the experiments were wild type *E.coli* K12 AW405. A single colony was picked from agar plate and cultured in 10 ml T-Broth (1 L of water, 10 g of tryptone and 5 g of NaCl) by rotating at 200 rpm for 16 h at 30°C. 20 μl of bacteria suspension was cultured again in 10 ml of T-Broth for 4 h until mid-exponential growing phase of *E.coli*. The bacterial suspension was washed three times by centrifuging at 2000 rpm for 8 minutes and re-suspending in fresh motility buffer (1 L of water, 11.2 g K2HPO4, 4.8 g KH2PO4, 0.029 g EDTA, 3.9 g NaCl; pH 7-7.5). The final suspension was diluted three fold before conducting experiments.

3.2.2 Polymer solutions

Ficoll 400 and Ficoll 70 have the same polymer structures, but different molecular weight. The molecular weights of Ficoll 400 and Ficoll 70 are 400,000 and 70,000, respectively. A 10% (w/v) stock solution of both Ficoll 400 and Ficoll 70 (Sigma-Aldrich) was prepared by dissolving the polymer in deionized water and rotating overnight at 200 rpm. The polymer solution was dialyzed for a week (Spectra/-Por 2 Dialysis Trial Kit, 12-14 kD MWCO, 23 mm flat-width membrane). The final polymer concentration was calculated by measuring the weight before and after evaporating the solvent for 6 h at 60°C and placing the solution for 4 h in vacuum until the final weight reaches a constant. The bulk viscosity of the solutions was measured using a rheometer (TA Instruments, AR2000) at different shear rates. Ficoll solution is known to be Newtonian [24] and our measurements confirm that the viscosity is

independent of shear rate.

3.2.3 Test fixture

The cell motion was observed using a test fixture consisting of a "swimming pool" cut from a 2 mm film of Polydimethylsiloxane (PDMS) sandwiched by a NO.1 glass slide and a NO1.5 glass cover slide.

3.3 Results and discussion

3.3.1 Speed distribution and skewness

A typical time history of speed and angular change (Fig. 3.1B, C) shows good qualitative and quantitative agreement with the classic results of Berg and Brown [7]. Using their definition of the run and tumble phases (Fig. 3.1A), we find that the run time and tumbling frequency are not affected by the fluid properties (Table 3.1). This is in contrast to the recent results of Patteson [32] who observed that both the mean run and tumble times increased with viscosity, suggesting that the frequency with the flagellar motor changes its sense of rotation decreases with viscosity. However, the CW and CCW motor rotation intervals are relatively insensitive to viscosity as long as the motor operates above a low speed nearing stall ($\omega > 50$ Hz) and below the no-load conditions ($\omega < 250$ Hz) [59, 60]. While the viscosity of the fluids considered by Patteson *et al.* was as high as 19 cP [32] - conditions that would put the motor frequency below 50 Hz - the present experiments were conducted in buffer solutions whose viscosity never rose above 5 cP (Table 3.1). In this regime, the motor rotation

speeds are quite moderate (Fig. 3.4A) and hence the motor reversal rates can be assumed to be independent of viscosity.

The change in fluid viscosity also has no effect on the change in orientation experienced during a tumble (Table 3.1). Although a more viscous fluid does imply a reduced angular diffusivity [22,61], the cell reorientation is an active, not passive event, driven by the splayed flagella pointing and rotating in different directions. During the tumble, a rotation of 1 radian is achieved in roughly 0.1 seconds (Table 3.1). In contrast, at the *lowest* viscosity, a 1 radian diffusive rotation ($t \sim \theta^2/2D_r$) [61] would take approximately fifty times longer. The detailed mechanics of the tumble remain a complex problem, particularly since one or more flagella might even have a different polymorphic shape (Curly, Semicoiled, Normal, etc.), depending on their sense of rotation and the applied torque [49].

A close inspection of the time-traces (Fig. 3.1B,C) indicates that the run-and-tumble description of motility may be too idealized to represent the observed swimming history; we see that a single cell exhibits both classical run-and-tumble events as well as periods of extended low-speed swimming or "slow-random-walk" [37]. This is quantitatively reflected by the probability density function (PDF) of the swimming speed during a single cell tracking sequence (Fig. 3.1D) which shows two peaks; one at high speed, which we associate with the observed run behavior, and a second peak at a lower speed, corresponding to the "slow-random-walk" behavior.

From these results, we assert that the "slow-random-walk" mode of motility is not the result of different cells illustrating different swimming modalities. Rather, over an extended period of time, a single cell can exhibit multiple modes of motility. Indeed, more complex combinations of speed and orientation changes are observed, (e.g. Fig. 3.1C, $t \approx 0$ - 4 seconds) which might be due to partial unbundling [48].

A valuable means to quantify differences between swimming behaviors is given by the shape of an individual cell's speed (U) distribution during a tracking sequence. In particular, the skewness, $K = \overline{(U - \overline{U})^3/\sigma^3}$, where bar denotes the mean value and σ is the sample standard deviation, is independent of the magnitude of the swimming speed and can illustrates a co-existence between run-and-tumble and "slow-random-walk" behaviors. One can imagine that a swimmer exhibiting a pure run-and-tumble behavior would have a PDF characterized by a sharp peak at the run speed with a broad low-speed tail. Such a speed distribution would have a negative skewness ($K < 0$). Similarly, a cell that spends more time in a tumbling state, with only short runs would have a low mean speed and a positively-skewed PDF ($K > 0$). Extreme swimming behaviors exhibited by mutant strains would also have characteristic speed distributions. For example, a "smooth" swimmer (one that does not tumble) would have a PDF with a peak at a high speed and zero skewness, while a "tumbly" swimmer - a cell that tumbles continuously - would have a speed distribution with a low mean speed and zero skewness.

The independence of the skewness to the magnitude of the average swimming speed is also of great value to the analysis of the data. Even though the average run times and tumble frequencies are relatively constant (Table 3.1), there is considerable cell-to-cell variation in absolute swimming speed (the standard deviation, σ, is approximately five times larger than the standard error bars plotted in Fig. 3.2A), most likely due to natural variations in the cell size, the length and number of flagella and/or individual variations in metabolic level. In addition, we observe that there is a marked difference between the swimming speed in dialyzed and native polymer solutions despite the fact that these solutions have the same bulk viscosity. Although the average swimming speed does decrease as viscosity rises, there does not appear to be a uniform behavior. The average swimming speed in native so-

Table 3.1: Run and tumble statistics in different polymers at different viscosities.

	Viscosity [cP]	Run time [s]	Tumble time [s]	Tumble angle [°]
MB 0.00%	0.93	0.88 ± 0.06	0.13 ± 0.01	71.72 ± 4.79
F70 1.67%	1.06	1.00 ±0.02	0.11 ±0.01	69.52 ±4.21
2.00%	1.11	0.85 ±0.02	0.13 ±0.01	74.01 ±3.11
2.22%	1.15	0.81 ±0.03	0.13 ±0.01	75.03 ±4.26
3.33%	1.24	0.83 ±0.09	0.14 ±0.02	74.30 ±2.33
6.67%	1.76	0.81 ±0.03	0.15 ±0.01	84.60 ±4.38
10.00%	2.52	0.92 ±0.04	0.14 ±0.01	68.84 ±5.10
F70Di 1.00%	1.01	0.96 ±0.04	0.11 ±0.02	70.37 ±4.13
2.50%	1.17	0.90 ±0.06	0.13 ±0.02	67.93 ±4.46
3.33%	1.24	0.89 ±0.08	0.12 ±0.02	69.95 ±5.58
5.00%	1.50	0.97 ±0.06	0.12 ±0.02	73.54 ±3.51
6.67%	1.76	0.86 ±0.05	0.11 ±0.01	64.88 ±4.78
10.00%	2.52	0.93 ±0.10	0.11 ±0.03	69.29 ±7.62
F400 0.83%	1.11	1.00 ±0.06	0.11 ±0.01	69.07 ±2.94
1.25%	1.17	0.99 ±0.11	0.13 ±0.02	65.42 ±3.57
1.67%	1.25	0.89 ±0.08	0.12 ±0.01	68.89 ±4.32
2.00%	1.32	0.91 ±0.13	0.14 ±0.01	78.84 ±4.50
2.22%	1.37	0.82 ±0.07	0.13 ±0.01	74.45 ±3.32
3.33%	1.61	0.99 ±0.11	0.13 ±0.01	73.93 ±6.19
6.67%	2.73	0.89 ±0.05	0.14 ±0.02	67.86 ±8.64
10.00%	4.85	0.89 ±0.10	0.14 ±0.02	73.99 ±4.19
F400Di 0.83%	1.11	0.95 ±0.10	0.11 ±0.02	60.20 ±4.38
1.25%	1.17	0.88 ±0.11	0.10 ±0.02	66.56 ±7.21
2.00%	1.32	0.80 ±0.11	0.11 ±0.02	65.14 ±3.77
3.33%	1.61	0.95 ±0.11	0.12 ±0.02	69.08 ±4.56
6.67%	2.73	0.92 ±0.10	0.12 ±0.02	70.43 ±3.41
10.00%	4.85	0.90 ±0.06	0.13 ±0.02	76.04 ±4.37

Table 3.1: Continued Run and tumble statistics in different polymers at different viscosities.

	Mean tracking time [s]	Number of cells
MB	14.49 ± 0.48	28
F70	16.63 ± 0.72	27
	14.37 ± 0.89	23
	19.46 ± 1.47	27
	18.41 ± 1.15	28
	18.56 ± 1.55	25
	15.36 ± 0.91	27
F70Di	17.42 ± 0.91	28
	18.07 ± 0.83	26
	17.87 ± 0.98	23
	17.13 ± 1.22	25
	18.41 ± 1.06	23
	15.84 ± 1.11	22
F400	16.38 ± 1.08	28
	16.74 ± 0.82	24
	14.52 ± 0.81	22
	13.34 ± 0.70	24
	16.27 ± 0.80	22
	15.12 ± 1.37	21
	14.19 ± 1.07	22
	14.98 ± 1.02	23
F400Di	14.41 ± 0.62	29
	14.06 ± 0.69	23
	14.81 ± 0.66	22
	15.13 ± 0.78	24
	16.53 ± 0.72	25
	16.30 ± 1.27	24

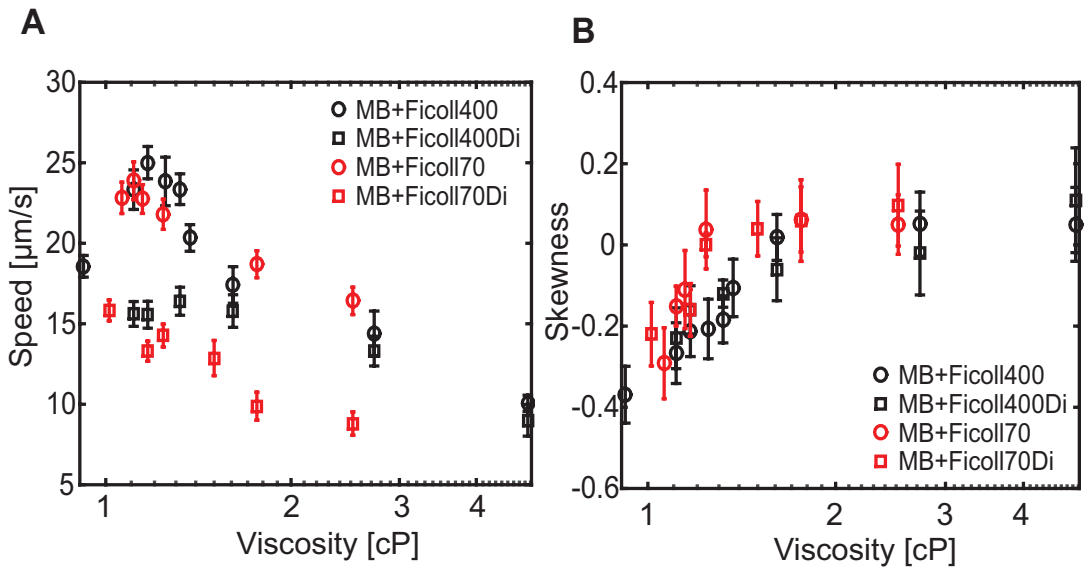

Figure 3.2: (A) Average swimming speed as a function of viscosity for Ficoll 400 and Ficoll 70 solutions (native and dialyzed). (B) Skewness of the swimming speed distribution as a function of viscosity. Although the average swimming speed exhibits variations as a function of the viscosity and the specific polymer solution, the skewness of the swimming speed distribution demonstrates a unified behavior, depending only on viscosity. The values is (A) and (B) are the mean ± one standard error ($\sigma/\sqrt{N}$). In the calculation of the mean speed and mean skewness, each bacterium is weighted equally. The average swimming speed of each bacterium is a time-averaged speed without trying to distinguish between run and tumble.

lutions increases initially before decaying, a phenomenon that has been previously observed [24, 58, 62]. However, in dialyzed solutions, the average swimming speed decays monotonically as viscosity rises. This discrepancy between average swimming speeds in native and dialyzed media was also observed by Martinez *et al.* [34] who attributed the difference to the presence of polymer fragments in the native solution that increase the baseline cell metabolic rate and motility.

Characterizing motility purely by the average swimming speed thus appears to be too blunt a tool; however, looking at the skewness of the speed distributions (Fig. 3.2B) we see that as the viscosity increases, the skewness changes monotonically reflecting a shift from a predominantly run-and-tumble style, characterized by a negative skewness, to a predominantly slow-random-walk style of swimming, characterized by a skewness close to zero. The same behavior is observed in all four

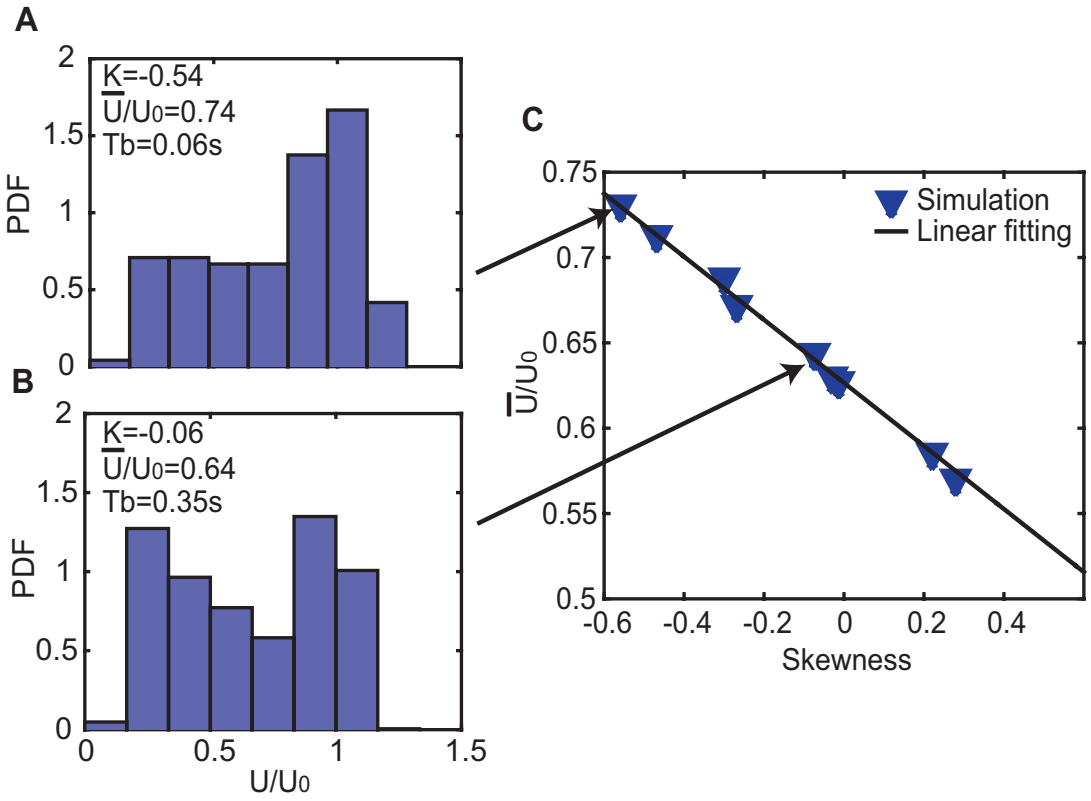

Figure 3.3: Idealized numerical simulations of swimming are defined by a characteristic run speed (U_o, held constant at 18 μm/s), a tumbling frequency (1 Hz) and a bundling time, T_b (varied, to simulate the effects of viscosity on the flagellar bundling process). The distribution of swimming speeds for (A) a "pure" run-and-tumble swimmer ($T_b = 0.06$ s, $K = -0.54$), and (B) a combined swimmer ($T_b = 0.35$ s, $K = -0.06$), show the effects of bundling time on the overall distribution. (C) A linear relationship is observed between the skewness of the swimming speed, K, and the ratio of the average speed to characteristic run speed: $\overline{U}/U_o = -0.185 \times K + 0.627$ (corresponding to 0.06 s $< T_b <$ 0.70 s).

polymer solutions (two different molecular weights, dialyzed and native solutions). This suggests that the *shape* of the speed distribution is a reliable fingerprint of the cell's swimming behavior, even while the mean value can show variability.

Note that the long-time speed histories of individual cells recorded using the tracking microscope provide the ability to generate these individual cell speed distributions. Population speed distributions, assembled by aggregating measurements from many cells [63, 64] will have a different shape.

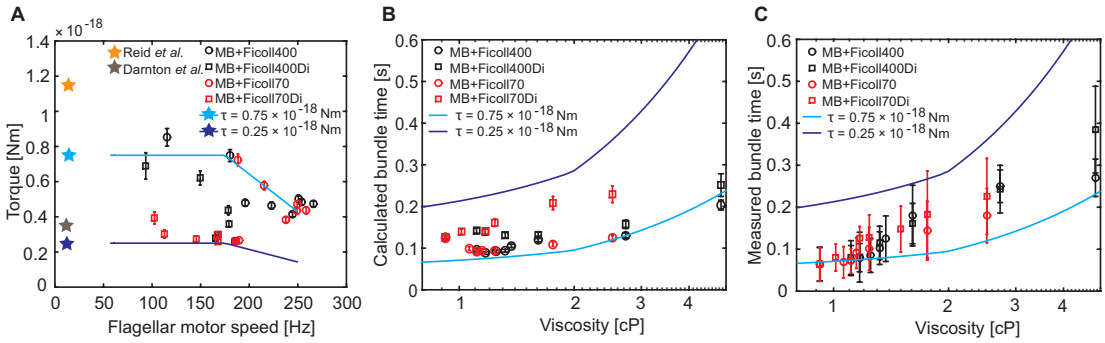

Figure 3.4: (A) Flagellar motor torque, calculated using RFT and using the measured characteristic run speed, U_o, and a typical cell geometry [58]. The blue solid lines are upper and lower bounds of the torque-speed characteristic, assuming a fixed "knee" speed at 175 Hz [65]. Previous motor torque measurement by Reid *et al.* [66] and Darnton *et al.* [49] are shown for comparison. (B) Calculated bundling time, T_b, as a function of viscosity. Here the calculations are based on RFT. Flagellar rotation rate ω_f is calculated using the characteristic run speed, U_o, determined from the skewnewss of the speed distribution from Fig. 3.3C. T_b is then calculated using ω_f under a fixed number of rotations. (C) Measured bundling time as a function of viscosity. The bundling time is calculated from the swimming histories. In both (B) and (C), the solid lines are calculated from RFT using motor torque characteristics given in (A).

3.3.2 The effects of viscosity on the bundling time

What might be the cause of this change in the swimming speed distribution? Assuming that the geometry of the cell body and flagellar filaments do not depend on the fluid viscosity, the hydrodynamics of the run scale linearly with viscosity [5,22]. Furthermore, the run and tumble durations are independent of viscosity (Table 3.1). However, the time for the flagellar bundle to unravel and reform during the tumble *does* change with viscosity. Kim *et al.* [26] showed that the flagellar bundling of elastic helices depends on a non-dimensional parameter, $M = \mu\omega L^4/EI$, where μ is the fluid viscosity, ω is the rotation rate, L the filament length, E the elastic modulus and I the moment of inertia. M represents the balance between the viscous and elastic stresses in the filament and Kim *et al.* demonstrated that flagellar bundling occurs after about 15 rotations for values of M greater than about 100. For a fixed torque motor [49, 65], the flagellar rotation rate will decrease as the fluid viscosity increases indicating that the bundling process, which requires a fixed number of

rotations [26] will take longer at higher viscosity. In addition, Turner *et al.* observed that the swimming speed of the cell remains depressed after tumble due to the rebundling process [14]. Thus it seems plausible that, as the viscosity rises, the cell spends less time running at full speed, and more time at lower speed recovering from tumbles. This hypothesis is consistent with our observation that the speed distribution skewness approaches or passes zero as the viscosity rises (Fig. 3.2B). The effect is obscured in the speed vs. viscosity data (Fig. 3.2A) by the confounding factors of individual variations in cell morphology and metabolic activity as well as the effects of polymers on cell activity level.

3.3.3 Numerical simulations

A numerical simulation confirms the relationship between the bundling time, the scaled average speed, and the skewness of the speed distribution. We model the swimming as a combination of a run at a given "characteristic run speed", U_o (18 $\mu m/s$), punctuated by tumbles that occur randomly. The acceleration from the tumble back to U_o is changed by the effect of varying viscosity on the bundling dynamics.

Synthetic swimming speed histories were created using a Matlab code designed to explore the connection between the bundling time and the skewness of the swimming speed distribution. The cell was assumed to swim with a characteristic speed of $U_o = 18$ μm/s. The duration of each run, in which all flagellar motors are assumed to be rotating in a CCW direction, is sampled from a exponential distribution [8,48] with an average run time of 0.86 s. [7]. Following the schematic in Fig. 3.1A, the tumble is modeled as a rapid deceleration in speed, from U_o to a tumble speed of $U_t = 5$ μm/s in 0.1 s. The cell remains at U_t for the duration of the tumble,

$T_t = T_1 - T_0$, sampled from an exponential distribution with a mean time of 0.14 s. The rebundling process, $T_{bsim} = T_3 - T_1 = T_b + 0.32 - T_t$, is modeled as a linear recovery in speed after tumble where 0.32 s is the duration of CW rotation [8,14,49]. Simulations were performed with T_b ranging from 0.06 to 0.70 s, mimicking the change in the viscosity. Characteristic run and tumble speed are held constant through the simulation since the statistics remain unchanged with linearly changed U_o and U_t as a result of change in viscosity. The run-tumble cycle is repeated to generate a time series lasting 2000 s. Finally, Gaussian white noise is added (1 dBW) to the entire series representing measurement uncertainty and diffusivity.

Using this idealized simulation, we generate synthetic speed histories and speed distributions associated with different bundling times (Fig. 3.3A, B) that are both qualitatively and quantitatively similar to the experimentally-measured distributions (e.g. Fig. 3.1D). From the simulated speed histories, we plot the distribution skewness against the ratio of the average swimming speed to the characteristic run speed, $\overline{U}/U_o$, and find that the data exhibits a linear trend: $\overline{U}/U_o = 0.627 - 0.185K$ Fig. 3.3C. More importantly, the simulation results allow us to use measurements of the speed distribution skewness, K, and the average swimming speed, $\overline{U}$, to estimate the characteristic run speed, U_o - a parameter that varies from cell to cell and is difficult to measure directly.

3.3.4 Evaluation of motor torque using Resistive Force Theory

Our approach follows Magariyama *et al.* [58]. However the details are reported here for completeness and convenience. For the force and torque on cell body we

have

$$\begin{bmatrix} F_b \\ \tau_b \end{bmatrix} = \begin{bmatrix} A_b & 0 \\ 0 & D_b \end{bmatrix} \begin{bmatrix} v \\ \omega_b \end{bmatrix} \tag{3.1}$$

and for the flagellum we have

$$\begin{bmatrix} F_f \\ \tau_f \end{bmatrix} = \begin{bmatrix} A_f & B_f \\ Bf & D_f \end{bmatrix} \begin{bmatrix} v \\ \omega_f \end{bmatrix}, \tag{3.2}$$

where F_b, F_f and τ_b, τ_f are the force and torque on the cell body and flagellum, v is the swimming speed of the cell. ω_b and ω_f are the rotation rate of the cell body and flagellum respectively. For the elements of the matrix in Equation 3.1, we assume that the cell body is a spheroid with length a and width b. The drag coefficient is a result of traditional low Reynolds number hydrodynamics [67] and is given as

$$A_b = -6\pi\mu\frac{b}{2}[1 - \frac{1}{5}(1 - \frac{a}{b})] \tag{3.3}$$

$$D_b = -8\pi\mu(\frac{b}{2})^3[1 - \frac{3}{5}(1 - \frac{a}{b})], \tag{3.4}$$

where μ is the viscosity of the fluid. The resistance matrix for the flagellum in Equation 3.2 is also a result of standard Resistive Force Theory (RFT) [58, 68, 69]:

$$A_f = \frac{2\pi\mu L \times (8\pi^2R^2 + p^2)}{[log(\frac{r}{p}) + \frac{1}{2}][4\pi^2R^2 + p^2]}, \tag{3.5}$$

$$B_f = \frac{2\pi\mu L \times (-2\pi R^2 p)}{[log(\frac{r}{p}) + \frac{1}{2}][4\pi^2 R^2 + p^2]} \tag{3.6}$$

and

$$D_f = \frac{2\pi\mu L \times (4\pi R^2 + 2p^2) r^2}{[log(\frac{r}{p}) + \frac{1}{2}][4\pi^2 R^2 + p^2]} \ , \tag{3.7}$$

where L is the length of the flagellar filament, p is the pitch the helix, R and r are the radius of the helix and filament respectively. The geometry of the cell body and flagellum used in our calculations is given in Table 3.2.

The coupled system is force free and torque free [5]:

$$F_f + F_b = 0 \tag{3.8}$$

and

$$\tau_f + \tau_b = 0 \ . \tag{3.9}$$

Table 3.2: Geometric parameters used in cell swimming calculations.

Symbol	Value
a	2.00 μm
b	0.60 μm
L	8.00 μm
p	2.00 μm
R	0.35 μm
r	0.03 μm

To solve for the swimming speed at a given viscosity, we assume a motor with the Torque-Speed, $\tau_m(\omega)$, behavior (Fig. 3.5):

$$\tau_m(\omega) = \tau_b = \begin{cases} \tau_{stall}, & \text{if } \omega \text{ ¡ } \omega_{knee} \\ \tau_o(1 - \frac{\omega_f - \omega_b}{\omega_o}), & \text{otherwise.} \end{cases} \tag{3.10}$$

This describes the motor torque behavior reported previously by Chen and Berg [65]

and used by Magariyama and Kudo [58]. If we assume $\tau_{stall} = 0.75 \times 10^{-18} N \cdot m$, $\tau_o = 1.5 \times 10^{-18} N \cdot m$ and $\omega_o = 350$ Hz [58, 65], we generate the light blue curve in Fig. 3.4 which serves as an upper bound for our calculations. However, there is debate about the value of τ_{stall}, and a smaller value, closer to that estimated by Darnton *et al.* [49], is given by $\tau_{stall} = 0.25 \times 10^{-18} N \cdot m$, $\tau_o = 0.5 \times 10^{-18} N \cdot m$, which generates the dark blue curve in Fig. 3.4 and provides a lower bound to our experimental results.

3.3.5 Evaluation of bundling time

With the estimate for U_o, and typical values for the geometry of the cell and flagella (Table 3.2), we use RFT to calculate the motor torque, τ, as well as the cell and flagellar rotation rate, ω_c and ω_f respectively. Although there is scatter in the data, the motor torque (at stall) is estimated to lie between 0.25 and 0.75 $\times 10^{-18}$ Nm (Fig. 3.4A), which agrees well with the measurement of Darnton *et al.* [49] who used a similar technique, but is lower than the measurement of Reid *et al.* [66]. It is worthwhile to note that the motor torque in the native polymer solutions is higher than the torque in the dialyzed solutions (Fig. 3.4A, circles and squares respectively), consistent with the observations both here, and by Martinez *et al.* [34] that the cell activity is generally higher in the native polymer solutions.

Using the motor torque and flagellar rotation rate obtained from RFT, we calculate the bundling time, $T_b = T_3 - T_2$ (Fig. 3.4B), assuming that 20 rotations are required for complete bundling. The results support the hypothesis that the bundling time is a function of viscosity, rising from approximately 0.1 seconds in pure motility buffer to about 0.2 seconds in the most viscous medium.

A second, independent, estimate of the bundling time can be found from the measured speed vs. time history of each cell. To accomplish this, we first use the skewness of the measured speed distribution to determine the characteristic run speed, U_o (Fig. 3.3C). Using Berg and Brown's definition of a change in angular orientation greater than 35°/0.08 s we identify the start of each tumble (T_o in Fig. 3.1A) and mark the completion of the re-bundling process as the time at which the swimming speed first reaches the characteristic run speed (T_3 in Fig. 3.1A). Since we do not measure T_2, we define the bundling time, T_b as $T_3 - T_o - 0.32$, where 0.32s is used as the duration of the CW rotation, $T_2 - T_o$ (Fig. 3.1A) [8, 14, 49].

The estimate of the flagellar bundling time obtained using this method (Fig. 3.4C) agrees well with the results obtained using RFT (Fig. 3.4B), demonstrating that the bundling time increases with viscosity, rising from about 0.08 to 0.3 seconds over the five-fold increase in viscosity. The scatter in the data likely results from our inability to accurately estimate the exact duration of the CW rotation, $T_2 - T_o$, and the variability associated with the determination of T_3.

3.3.6 Flagellum length changes

As the surrounding fluid viscosity increases, the flagellar filament might deform due to the hydrodynamic force and this deformation would change our calculations. To estimate the length change we first estimate the extensional stiffness of the flagellum. From Figure 4 of Darnton *et al.* [70], we estimate the linear compliance near zero extension, $\delta x/\delta F$, to be

$$\left.\frac{\delta x}{\delta F}\right|_{x=0} \approx \frac{3}{10}\frac{\mu m}{pN}. \tag{3.11}$$

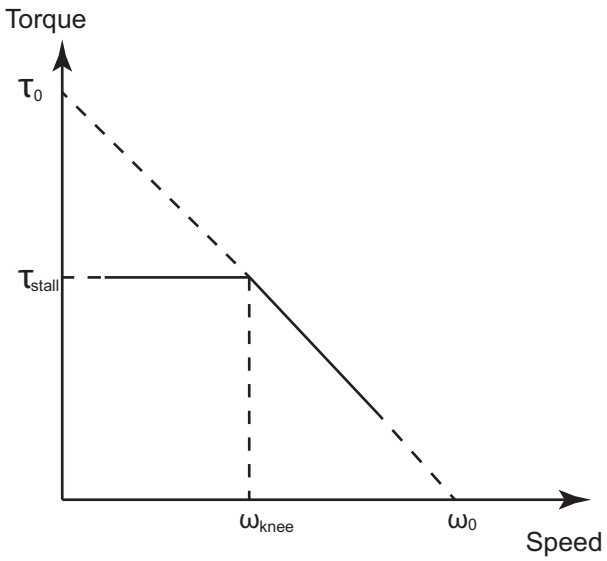

Figure 3.5: Typical flagellar motor torque speed relation [65]. Motor torque is constant for $\omega < \omega_{knee}$, after which it decreases linearly to ω_o.

The hydrodynamic force on flagellum is, at most, given by the drag force experienced by the cell body (Equation 3.1 and 3.3). The largest viscous drag coefficient A_b under our experimental condition is approximately $-4.0 \times 10^{-8}\ Ns/m$ ($\mu = 4.9$ cP; a, b given in Table 3.2); the velocity, v, is 10.0 $\mu m/s$ and the estimated drag force is $\sim 0.4\ pN$. Using this, and the extensional compliance, Equation 3.11, we estimate that the largest change in flagellar length would be $0.5 \times 0.3 \times 0.4 = 0.06\ \mu m$ which is much smaller than the total filament length of 8 μm[1]. We conclude that it is safe to ignore this effect and assume a constant geometry.

[1]Note the 0.5 in calculating the change of flagellum length uses the fact the force acting on the flagellum balanced by the drag force on cell body is evenly distributed through the flagellum, not a point force applied at the tip.

3.3.7 Mean square displacement of wild-type *E. coli*

The mean square displacement MSD, defined as

$$MSD \equiv < (x - x_o)^2 >= \frac{1}{N} \sum_{i=1}^{N} (x_i(t) - x_i(0))^2, \tag{3.12}$$

is widely used to characterize low Reynolds number swimming phenomena [32,71,72]. The motion of a particle undergoing random diffusion exhibits a MSD that increases linearly with time [73]:

$$MSD = 6Dt \tag{3.13}$$

where D is the effective diffusion constant. In contrast, a ballistic swimmer with a constant speed, c, exhibits an MSD that increases quadratically in time:

$$MSD = c^2 t^2. \tag{3.14}$$

The MSD of the *E. coli* measured in our experiments are shown in Fig 3.6 for all cells swimming in native Ficoll 70 of different viscosities. Ballistic behavior is observed for short times while diffusive behavior is seen for times greater than about $t = 1$ second, in consistent with previous observation by Patteson *et al.* [32]. There is no observable dependence on viscosity of the crossover time between ballistic and diffusive behavior, consistent with our observation (Table 3.1) that the run times are independent of viscosity. Similar MSDs are obtained for all four media tested (Ficoll 70, Ficoll 400, both native and dialyzed).

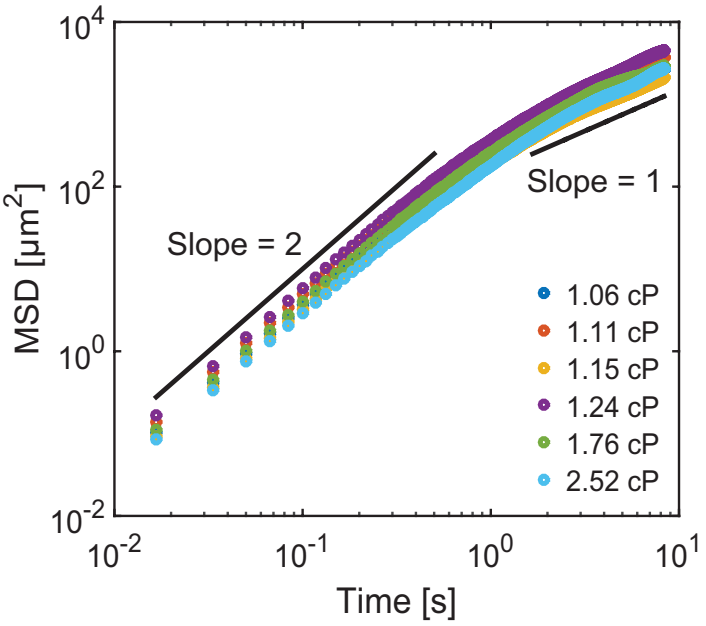

Figure 3.6: Mean square displacement of the swimming cells with respect to time at different viscosities in native Ficoll 70 solution. Each data point is averaged over 15 individuals.

3.3.8 Population speed distributions

The speed distributions for all cells are shown for three viscosities in Fig. 3.7 A1, B1 and C1. This includes all cells tracked at this viscosity for a given buffer (in this case, dialyzed Ficoll 400). The shape of the PDFs is in agreement with previously reported population speed distributions [63,64] (measured using statistical techniques, not using long-time tracking of individual cells). Fig. 3.7 A2,B2 and C2 show the corresponding *normalized* speed distributions in which each individual cell's speed history is divided by its characteristic run speed, U_o (Fig. 3.1) before combining to compute a population speed PDF. As discussed in the main text, the normalization accounts for individual variations in average swimming speed due to cell and flagella size and metabolic activity. As the viscosity rises, the change in the skewness of the normalized population PDFs is evident, corroborating the result shown in Fig. 3.2B, which is the same data, but plots the average of the skewness of each individual cell's speed distribution.

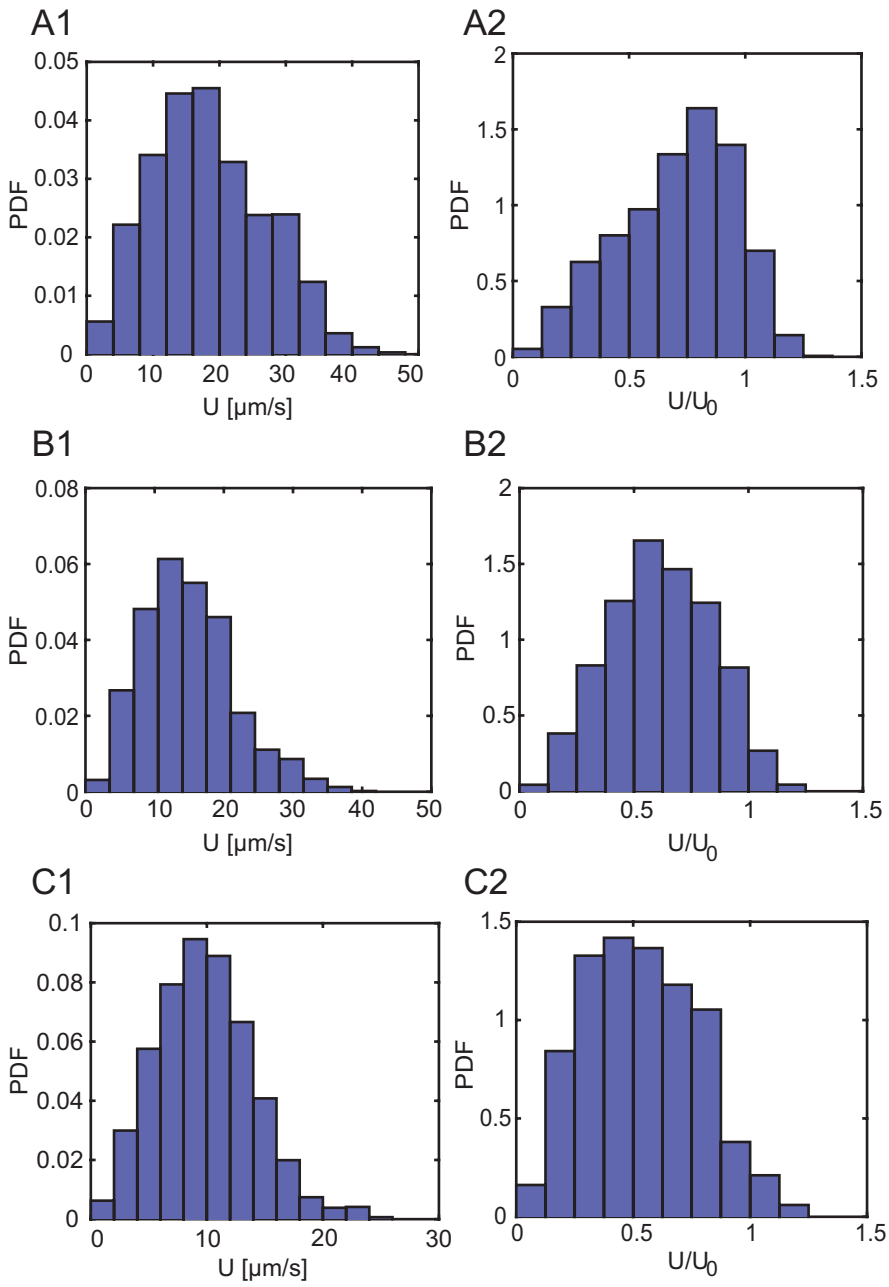

Figure 3.7: Left column, the un-normalized speed distribution of all individuals tested at a given viscosity. (A1) $\mu = 0.93$ cP, (B1) $\mu = 1.61$ cP, (C1) $\mu = 4.85$ cP. All three plots show a similar distribution as suggested by [63, 64]. Right column, the corresponding normalized (by the characteristic run speed of each individual) speed distribution, a clear transition from negative skewness in (A2) $K = -0.37$, to a intermediate skewness in (B2) $K = -0.05$ and finally a positive skewness $K = 0.18$. This transition is observed in Fig. 2B as the increase of average skewness with respect to viscosity.

3.4 Summary and conclusions

We have shown that the motility of a wild-type *E. coli* cell is quite nuanced, exhibiting both run-and-tumble and slow-random-walk modes of locomotion. The balance between these natural swimming behaviors can be quantified using both the average speed, $\overline{U}$ and the skewness of the speed distribution, K. A distinct feature of the skewness is that it is independent of differences in the characteristic run speed that arise due to cell-to-cell variations and the uncontrolled presence of biological stimulants in the surrounding medium.

We believe that these results clarify some of the confusion surrounding cell motility in viscous media by demonstrating that the swimming *behavior* changes as the viscosity rises due to the fact that the flagellar bundling process takes longer at higher viscosity slowing the rotation of the flagellar motors. Future experiments, theory and simulations, including using viscoelastic media [32, 34, 51, 55, 57] and visualizing the flagella [14, 48] will be critical in providing a full understanding of this mechanism.

Chapter Four

Characterizing the viscoelastic behavior of dilute polymer solutions using microrheology

4.1 Introduction

The rheology of complex fluids has been studied extensively through the last few decades [74–76]. It is highly related to not only industrial applications, such as paints [77], plastics [78] and printing inks [79], but also to many research areas especially on biological application and processing [80, 81]. The rheological properties, especially viscoelasticity of complex fluids, give important details on micro-structural features and dynamics of the system [82]. In general, the relaxation time of the system varies and spans over a wide range of time scales depending on this viscoelastic moduli (G' and G'') [83, 84]. For dilute polymer solutions with small molecule sizes, the relaxation time is usually short. Measurements with high frequency are indispensable to resolve their rheological behavior [85, 86].

The viscoelastic behavior of such solutions can be measured using an oscillating shear rheometer [87, 88], which however requires a precise and sensitive measurement of the torque of the shear plate at a high frequency and is difficult to achieve using a conventional rheometer [88]. Microrheology based on the particle dispersion in non-Newtonian solutions has been previous proposed [85, 89] to overcome such difficulties. The typical experimental technique in microrheology for resolving the statistics of the particle displacement is Dynamic Light Scattering (DLS) [89]. However, the experimental system includes a monochromatic light source, usually a laser plus additional specialized equipment [90] which makes it hard and expensive to implement. Measuring particle dispersion from regular fluorescence microscopy is challenging at high sampling frequency ($\sim$ 500 Hz), which however is necessary in resolving the viscoelastic behavior of dilute polymer solutions [84].

The most general way of measuring particle displacements or mean square dis-

placement (MSD) is by calculating the position differences of the same particle in consecutive images. However, the positions of fluorescent particles are difficult to detect accurately with short exposure at high frame rate. Camera noise, especially generated from the CMOS camera, including the general Gaussian noise [91], photon shot noise [92] and signal read noise, becomes severer as the image acquisition frequency increases. Image intensifier is capable of detecting and amplifying low-light-level images to overcome the limited exposure at high frame rate for fluorescent systems [93], however it brings additional noise to the resultant image. All these noisy signals may lead to a false measurement of particle displacements during image post-processing. In addition, not only optical noises, overlapping due to particle dispersion itself could also bring difficulties in displacement detection [38].

Another drawback of traditional particle displacement detection is that it requires a precise particle-to-particle matching between frames. The most widely used algorithm for particle matching is nearest-neighbor matching [94], which however does not guarantee a correct match and gets worse with all the false signals introduced at high frequency. Even in dilute particle suspensions, it is possible that multiple particles cluster locally and the nearest-neighbor algorithm does not lead to a one-to-one matching. Particles may also disperse out of focus or outside the observation window so that a particle pair is not physically exist. For images taken at high frequency, some background noise can be detected as "particles" and such random appearance breaks the one-to-one matching using nearest-neighbor algorithm.

To address these issues when measuring the MSD at high frequency, Statistical Particle Tracking Velocimetry (SPTV) technique [38] is applied on the image and data post-processing. With a similar approach, SPTV requires all particles in each frame to be detected using intensity threshold [36] or diffraction ring [95]. Instead of finding a precise particle matching, SPTV purposely utilizes a large interrogation

window to include multiple tracer particles (and noise "particles") and measures the displacement distribution. Drop-in/drop-out particles due to dispersion and noise "particles" are all included for particle matching to generate the statistics but eliminated later by exploiting the nature of correct particle matching [38]. Therefore, we used SPTV as suggested by Guasto *et al.* [38] to overcome the difficulties when implementing traditional particle displacement measuring techniques.

In this paper, we present our study on the measurement of viscoelastic behavior of Methocel 90 HG solutions at various concentrations with low shear viscosities (up to 18 cP) and weak elasticities using microrheology. SPTV is applied in data processing for the MSD measurement at different frequencies.

4.2 Experimental setup and procedure

The schematic of the experimental configuration is shown in Fig. 4.1. A 0.500% (wt/vol) Methocel 90 HG stock solution was prepared by dissolving the polymer in deionized water and rotating overnight at 200 rpm. Lower concentration solutions were diluted from stock solution. The particle suspensions were prepared by diluting the fluorescent beads (Molecular Probes, 200 nm, 540/560) 500,000 times into polymer solutions at various concentrations. Paraffin film (Parafilm M) was cut into squares ($\sim$ 1 cm) and punched with a hole ($\sim$ 0.3 cm) in the middle. It was gently put upon a NO.1 coverglass (Fisher Scientific) and loaded on a heat plate (Cole Parmer) for 30 s until the film was melting. A small volume (50 μL) of the test fluid was placed in the middle of the film hole and sealed by a NO.1.5 coverslip (Fisher Scientific) on top. The sample was cooled down at room temperature for 5 min before experiment. The motion of the particles was observed using an inverted mi-

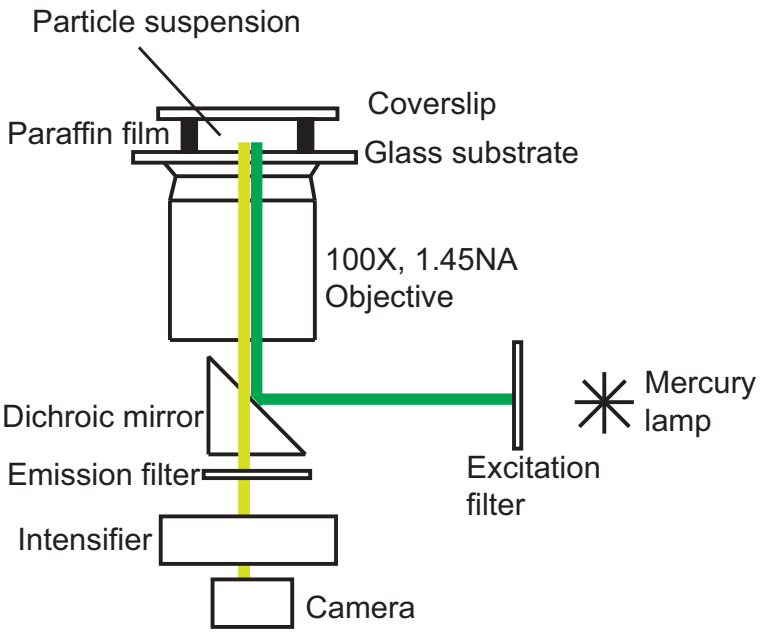

Figure 4.1: Schematic of the experimental configuration. The tracer particles are illuminated using a mercury lamp with excitation filter, the beam is introduced along the optical axis. The emission light follows the same light path until it reaches the dichroic mirror and passes through the emission filter. The light is captured via an image intensifier by a CMOS camera at up to 1000 fps.

croscope (Nikon ECLIPSE TE2000-U) equipped with a 100X oil immersion objective (Nikon, Plan Apo TIRF). Images were recorded using a high speed CMOS camera (Photron Fastcam SA-5) fitted with a high-speed image intensifier (Hammamatsu V9501U-74-G240).

In order to resolve the frequency-dependent viscoelastic moduli of the polymer solutions at various concentrations. Images were recorded at different frequencies [89] ranging from 5 Hz to 1000 Hz using Photron FASTCAM Viewer (PFV) software. 2000 images were saved for each sample suspension and each experiment was repeated 3 times to reduce measurement errors and to ensure consistency.

4.3 Image analysis and data processing

Images were processed using custome software written in C++ and using the OpenCV library. A bilateral filter [96] was applied to the image to reduce background noise. This filter was used since it reduces the noise without sacrificing the sharp intensity gradient near edges [97]. Following the filter, the positions of particles (along with any leftover background noise) were detected using the *contour* and *moment* functions in the OpenCV library. An interrogation window with size l, centered with an arbitrary particle was assumed. The displacements between the central particle and all particles detected in the following image within the same interrogation window was calculated and recorded (Fig. 4.2). All displacements between consecutive images were calculated by applying interrogation window on all particles in the first image. Then the whole displacements histogram was generated by repeating the same procedure to the complete image sequence.

As suggested by Guasto *et al.* [38], the distribution of particle displacement in the i-th direction ($i = 1, 2$) $\Delta x_i(t)$ should have the form of a modified Gaussian distribution with zero mean:

$$S_i(x,t) = C_i(t) + \frac{1}{\sqrt{2\pi\sigma_i(t)}} \exp(-\frac{(x-\mu_i(t))^2}{2\sigma_i(t)^2}), \tag{4.1}$$

which is simply a Gaussian distribution plus a constant offset, or "table". The Gaussian part is due to the correlated particle displacements [98] while the table derives from the un-correlated particles and particle-noise correlation [38], which are random and have uniform distribution. Note that the MSD of particle dispersion is defined as

$$MSD_i(t) =< (x_i(t) - x_i(0))^2 >=< (x_i(t))^2 >, \tag{4.2}$$

and by definition, the standard deviation $\sigma_i(t)$ of the Gaussian part in Equation 4.1 is given as

$$\sigma_i(t) = \sqrt{< (x_i(t) - \mu_i(t))^2 >}. \tag{4.3}$$

$\mu_i(t)$ quantifies the mean speed of the flow field and in our case it is close to 0. $\sigma_i(t)^2$ is then a good estimation of $MSD_i(t)$.

The measured displacements histogram is fitted using Equation 4.1 to retrieve the MSD in the x and y directions. The size of the interrogation window (l) is chosen to be larger than at least three times $\sigma_i(t)$ for each fitting process. The MSD is often overestimated in this case when $l < 3\sigma_i(t)$.

4.4 Results and discussion

Sample images are shown in Fig. 4.2 illustrating randomly seeded particles (diameter: 200 nm) in 0.125% Methocel solution. Fig. 4.2 A1 and A2 are two consecutive images taken at 250 fps, while images B1 and B2 are zoomed-in parts of each image denoted by the red squares, illustrating the interrogation window.

Following the statistical particle tracking process [38], the displacement distribution is generated and shown in Fig. 4.3 as the green histograms. It is noted that the distribution, shown by the fitted curve in a solid line, follows a Gaussian distribution plus a constant [38]. The same data is processed choosing three different interrogation window sizes. A, $l = 0.2$ μm. B, $l = 0.3$ μm. C, $l = 0.5$ μm. The standard deviation of fitted curve in A is 0.108, while 0.097 and 0.098 in B and C respectively. This demonstrates the effect of interrogation window size l on fitting result. It is observed previously that for particle dispersion in non-Newtonian flu-

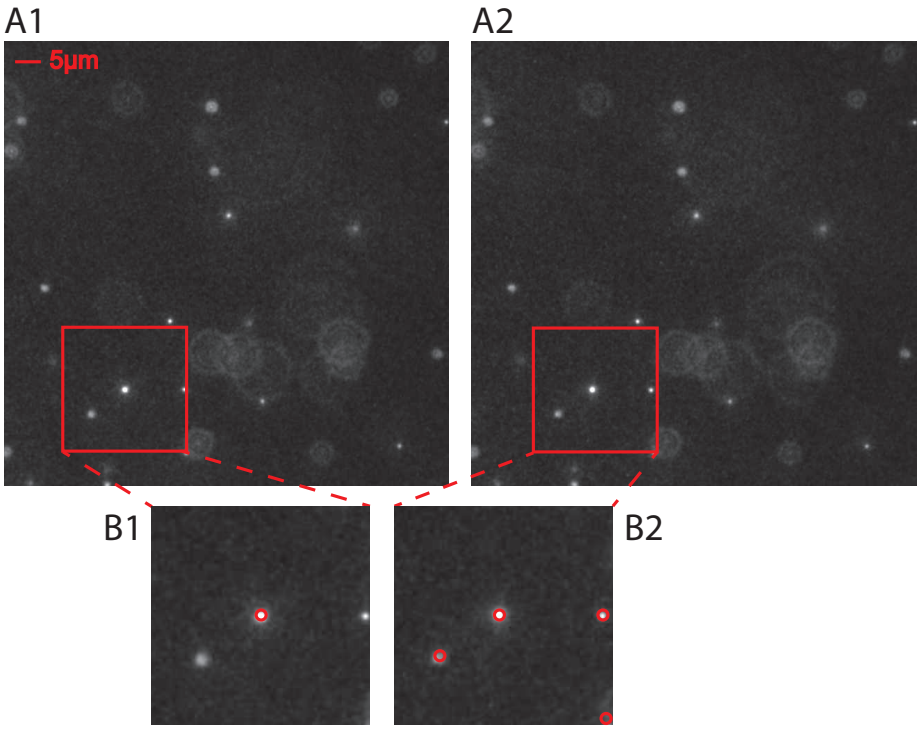

Figure 4.2: Particles (200 nm) dispersion in 0.125% Methocel solution at two consecutive frames (A1 and A2). B1 and B2 are zoom-in images of the parts shown in A1 and A2 by a square (interrogation window) respectively. The circle marker in B1 shows the central particle and markers in B2 are all particles detected within the same interrogation window in the following image. The displacements are measured between all particles in B2 to the one in B1.

ids, the displacement distribution forms a Gaussian center plus a non-Gaussian tail, especially for the case when observation time is close to relaxation time [99, 100]. However, the non-Gaussian tail contributes around 5% to the total distribution as suggested by Weeks *et la.* [99], which brings a subtle change in the estimated MSD compared with the one by assuming a Gaussian distribution.

Measuring the MSD of dispersive particles is the first step in resolving the viscoelastic behavior of complex fluids such as polymer solutions [84,101]. In Newtonian solutions, the MSD of diffusive particles increases linearly with respect to time [102] which is observed in our system and shown in Fig. 4.4. Particles with two sizes (100 nm and 200 nm) are seeded in water, the resolved MSD show a good agreement with theoretical approximation [102] denoted by the solid lines. Then the MSD of 200

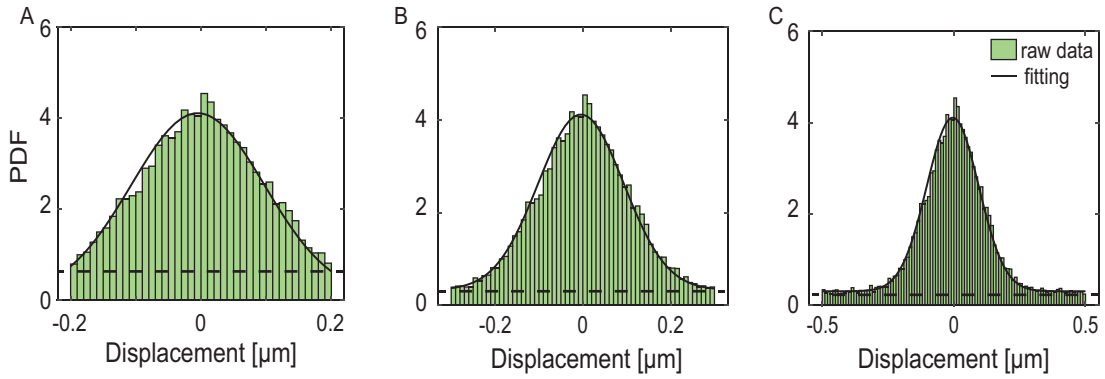

Figure 4.3: Measured displacement distributions of 200 nm dispersive particle in 0.125% Methocel solution. The green histogram is the experimental data and the fitted curve is generated using a least square non-linear fitting using a model equation given in Equation 4.1. The constant of the fitting result is marked by the dashed line which distinguished the particle diffusion result from the noise and un-correlated particle displacement. The same data is processed choosing three different interegation window size. A, $l = 0.2$ μm. B, $l = 0.3$ μm. C, $l = 0.5$ μm.

nm particle in non-Newtonian solutions at different concentrations are measured and calculated as shown in Fig. 4.5. It is observed that the MSD decreases as the polymer concentration increases, indicating an increased viscous behavior. The slopes of MSD over time at longer time are 1 in logarithm scale [85] for all concentrations used in the experiment, suggesting a predominating Newtonian behavior. The slope becomes less than 1 at shorter time scale, suggesting the existence of elastic behavior. Moreover, it is directly observed from Fig. 4.5 that the crossover time (relaxation time), which is indicated by the transition point when the slope of the curve becomes less than 1 increases with respect to polymer concentration.

The relaxation time τ_i and viscoelatisc moduli G', G'' (Fig. 4.6) are calculated following the method given by Mason *et al.* [85]. In general, the relaxation times τ_i are chosen logarithmically to cover the desired range of s [54, 85]. The fitting result in Table 4.1 shows that there is no significant difference between the cases of $i = 1$ (single relaxation time) and $i > 1$ (multiple relaxation times).

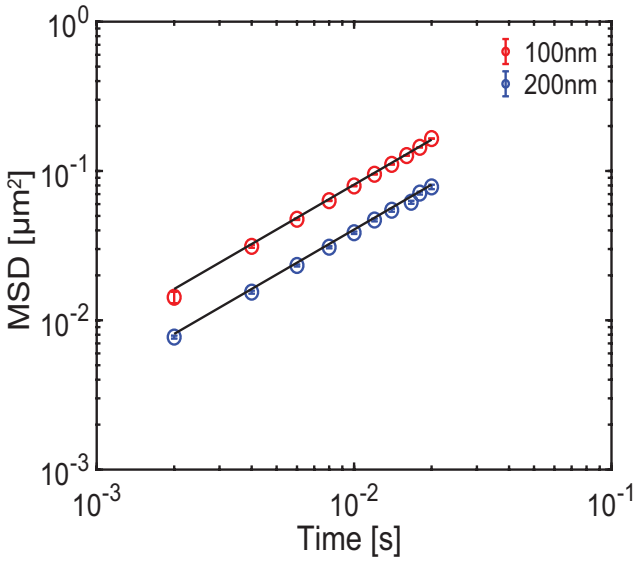

Figure 4.4: MSD of diffusive particles in water. Particles with two sizes (100 nm and 200 nm) are tested to calibrate the measurement and processing algorithm. The black lines are estimated MSD over time theoretically using Stoke-Einstein equation. Temperature is 18°C.

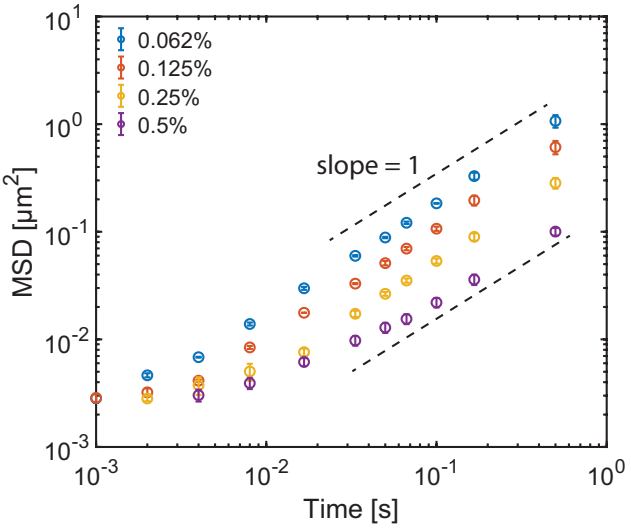

Figure 4.5: MSD of particle dispersion in Methocel solutions at different concentrations as a function of time. The slope of MSD over time is 1 in four different concentrations at long time scale and becomes less than 1 at short time scale. In addition, the transition time increases with respect to polymer concentration.

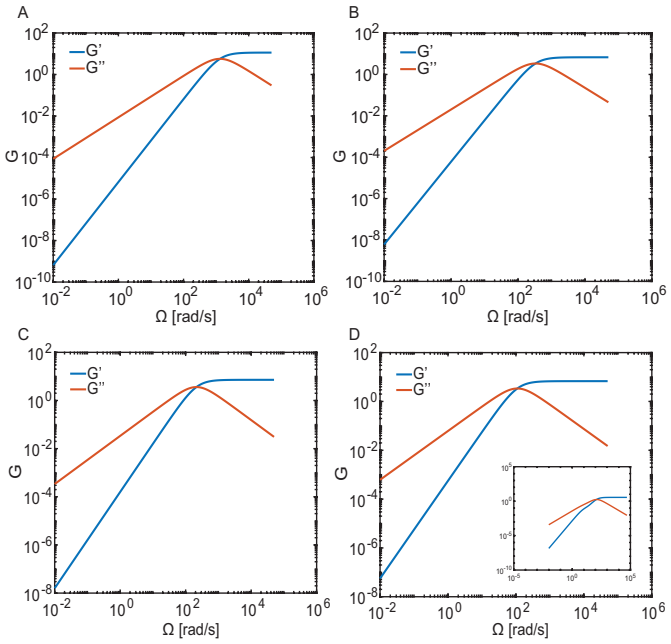

Figure 4.6: Calculated elastic and viscous modulus of the Methocel solutions tested in the experiment at different concentration. A, 0.062% B, 0.125% C, 0.250% D, 0.500%. The non-linear fitting model assumes a single relaxation time as it is similar to the result of multiple relaxation time. The cross over point, which also indicates the relaxation time increases as a function of polymer concentration which is observed from Fig. 4.5.

Table 4.1: Relaxation time of Methocel solutions at varying concentrations.

	Concentration	τ_1 [ms]	G_1		
	0.063%	0.76	11.34		
i = 1	0.125%	2.99	6.76		
	0.250%	4.68	7.23		
	0.500%	9.00	3.39		
	Concentration	τ_1 [ms]	G_1	τ_2 [ms]	G_2
	0.063%	0.76	11.34	1.00×10^{-9}	1.00×10^{-3}
i = 2	0.125%	3.13	6.65	4.53×10^{-6}	3.13×10^{-3}
	0.250%	4.70	7.20	2.42×10^{-5}	1.92×10^{-2}
	0.500%	8.99	3.46	5.43×10^{-4}	6.52×10^{-6}

4.5 Concluding remarks

Statistical Particle Tracking (SPT) has been introduced and applied to a microrheology experiment as a replacement of more conventional tracking techniques. The advantages of SPT are that it removes concerns of spurious particle tracking which is particularly problematic when tracking small particles with highly-amplified intensified images. The data presented here demonstrate that the sampling frequency of microrheology measurement with intensified high speed image acquisition and fluorescent microscopy works up to 1 kHz. It thus extends the measured spectrum of a conventional mechanical shear rheometer. The result indeed shows that the relaxation times of dilute Methocel solutions, which are on the order to 10 ms, are short. Our result provides a robust basis for a complete study of the viscoelastic behavior of dilute polymer solutions.

Despite its appeal, this method is still limited. First, the rheology of the fluid is resolved at zero shear rate. Second, for solutions with higher viscosity, smaller-sized particles (or quantum dots) are needed for displacement detection [38], which may not be guaranteed to observe the Stokes-Einstein relation even in Newtonian solutions [38]. Lastly, the SPT method requires a known physical distribution which makes it difficult to implement on particle dispersion in concentrated polymer solutions, where the distribution is non-Gaussian [99, 100].

4.6 Materials and methods

4.6.1 Polymer solutions

Methocel 90 HG, also known as Hydroxypropyl Methylcellulose (HPMC) type K was used in this experiment. A 0.5% (w/v) stock solution of Methocel 90 HG (Sigma-Aldrich) was prepared by dissolving the polymer in deionized water and rotating overnight at 200 rpm. Methocel solutions are formally known to be non-Newtonian [24] at high concentration with elastic behavior. Most previous research resolved the rheology behavior of Methocel solutions at high concentration [103] while our study focused more on the rheology of dilute Methocel solutions.

4.6.2 Test fixture

The particle suspension was observed using a test fixture consisting of a micro channel made by heating a paraffin film (Parafilm M) punched with a hole in the middle on top of a NO.1 glass slide and then covered with a NO1.5 glass cover slide.

4.6.3 Non-linear curve fitting for displacement distribution

A non-linear curve-fitting based on Equation 4.1 is applied on the histogram from the experimental data. The fitting is processed using Matlab (MathWorks) using $fitnlm$ function. An demonstration of the fitting is shown in Fig. 4.3 black curves, the standard deviation $\sigma_i(t)$ of the Gaussian distribution is retrieved directly from the fitting result.

4.6.4 Viscoelastic spectrum calculation

To accurately measure the relaxation time (τ), we follow the method proposed by Mason *et al.* [85]. Assuming the fluid is isotropic and incompressible, the fluids viscoelastic spectrum $\widetilde{G}(s)$ is calculated using Equation 4.4.

$$\widetilde{G}(s) \approx \frac{k_B T}{\pi r MSD(t)\Gamma[1 + (\partial ln(MSD(t))/\partial ln(t))]}\Big|_{t=1/s} \tag{4.4}$$

where k_B is the Boltzmann constant, T is the absolute temperature, r is the radius of the particle and Γ stands for Γ function. We calculate the fluids viscoelastic spectrum $\widetilde{G}(s)$ using the result from Fig. 4.5. The partial derivative is numerically approximated using the first order finite difference. A non-linear curve fitting of $\widetilde{G}(s)$ to Equation 4.5 with a least-squares routine is performed to find the relaxation time τ_i:

$$\widetilde{G}(s) = \sum_i \frac{G_i s}{s + 1/\tau_i}. \tag{4.5}$$

The storage (G') and loss (G'') modulus for polymer solutions at different concentration using a single relaxation time are calculated using Equation 4.6 and 4.7 and plotted in Fig. 4.6. The inset of Fig. 4.6 D is the same viscoelastic moduli as plotted in D but with two relaxation times.

$$G'(\Omega) = \sum_i \frac{G_i \tau_i^2 \Omega^2}{1 + \Omega^2 \tau_i^2}. \tag{4.6}$$

$$G''(\Omega) = \sum_i \frac{G_i \tau_i \Omega}{1 + \Omega^2 \tau_i^2}. \tag{4.7}$$

Chapter Five

Non-Newtonian effects change flagellated bacteria motility

5.1 Introduction

Many microorganisms propel themselves by rotating rigid helical flagella [7] or undulating flexible cilia [23, 104]. The physics of swimming at low Reynolds number in both viscous and non-Newtonian fluids has been studied extensively not only for its implications in Engineering [105–107], such as on the design of microrobots [108], but also for the insight into many aspects of natural science. For example, low Reynolds number swimmers provide experimental models for the study of active suspensions [109].

Flagellated bacteria lived in various aquatic environments and many of these biological fluids, such as mucus [110], are complex non-Newtonian fluids. One particular area in low Reynolds number problem that has been recently focused on is to understand swimming behavior in such fluids. Flagellar locomotion in non-Newtonian fluid received lots of attention primarily on theoretical and numerical perspectives. One of the early work done by Lauga [51] showed that the translational speed of Taylor Sheet [111] decreased with the appearance of viscoelastic effects. Similarly, Fu *et al.* [52] demonstrated that the swimming speed of a rotating helix of small amplitude was slowed down by elastic stress. However, recent studies have also shown that viscoelasticity can lead to an enhanced locomotion. Spagnolie *et al.* [55] performed numerical simulations on rotating helical swimmers with varying geometry in an Oldroyd-B fluid [112] and discovered that the swimming speed can be enhanced for certain geometries over a range of Deborah numbers $De = \omega_f \tau$, where ω_f and τ were the rotation speed of the helix and the relaxation time of the fluid. Riley and Lauga [113] found the swimming speed for modified Taylor Sheet, which included multiple superposed traveling waves, was enhanced in viscoelastic fluid. In addition, inelastic shear-thinning effects have also been shown to play a

significant role in changing the swimming speed. Montenegro-Johnson *et al.* [114] studied two-dimensional swimmers in generalized Stokes flows and found that even with identical morphological swimmers, the swimming speed could be either enhanced or hindered, depending on the flagellar locomotion (strokes), the swimming speed was very sensitive to the kinematics. Similarly, Datt *et al.* [115] studied a three-dimensional squirmer in a shear-thinning fluid using a combination of numerical simulations and asymptotic analysis and found that the change in swimming speed was non-monotonic and depended on surface actuation.

Experiments have also been conducted to explore the complex swimming behavior of living cells in non-Newtonian solutions. One of the earliest results was presented by Berg and Turner [24] who measured the rotational speed of wild type tethered *E.coli* and discovered a non-monotonic change in rotational speed as a function of viscosity. In addition, the rotational speed was different in Ficoll (branched polymer, Newtonian) and Methocel (unbranched polymer, non-Newtonian) solutions, even in the media exhibited the same bulk viscosity. They concluded the difference was due to the interactions between flagellar filaments and the quasi-rigid polymer networks. More recently, experiments have been designed to measure the effects of both the viscoelastic and shear-thinning on bacteria swimming speed. Patteson *et al.* [32] tracked wild type *E.coli* in viscoelastic polymer solutions and found that the cells swam faster with increased elasticity. They concluded this speed enhancement was possibly due to the shear-induced normal stress acting on the cell body, forcing the cell to swim straighter at a higher efficiency.

E.coli cells swim by rotating multiple flagellar filaments [7] and form a flagellar bundle, which can be modeled as a single rigid helix [33, 49, 58]. In the low Reynolds number regime, the force and torque imposed on the cell body are balanced with the force and torque generated by the flagella [23]. Thus, to balance the torque from the

flagella the cell body of bacteria *E.coli* is also rotating as it swims but in the opposite direction compared to flagella. In general, since the flagellar motors are randomly distributed on the cell body [8], it is unlikely that flagellar bundle and cell body orient perfectly in the same direction as it propels through the fluid. It has been shown that this off-axis configuration (shown in Fig. 5.1 angle ϕ) results in a wobbling trajectory as the cell swims in Newtonian solutions [49, 116]. The shear flow generated by the rotating cell body leaded to a normal force pointing inwards the centerline of the cell and reduced the wobbling effect, which thus improved the swimming efficiency and resulted to a enhanced swimming speed. However the swimming speed of *C.elegens*, which undulated itselt to navigate through the fluidic environments, was observed to be decreased with elastic stress by Shen and Arratia [117]. Meanwhile, swimming speed of *E.coli* cells [34] was tested by Martinez *et al.* in shear-thinning fluids and a speed enhancement was observed.

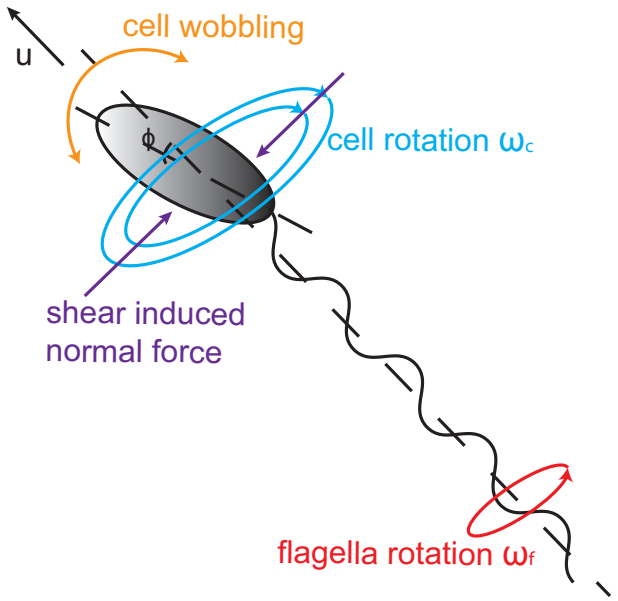

Figure 5.1: Schematic of bacteria *E.coli* swimming in non-Newtonian solutions. Shear-induced normal force generated by the rotational flow around cell body points inward and is perpendicular to the swimming direction.

Evidently, results from theoretical, numerical and experimental perspectives remain controversial and there is still no clear understanding of the relatively impor-

tance of non-Newtonian effects on swimming behavior. Three non-Newtonian effects have been proposed to explain the speed change in polymer solutions: shear-induced normal force [32], elasticity [54, 55] and shear-thinning effect [34, 118]. In particular for the experimental results that use *E.coli* [24, 32, 34], a wild type strain, which is known to have a "run and tumble" motility [7], was used. It has been shown previously by Qu *et al.* [33] that the flagellar bundling process of a wild type swimmer during tumble is very sensitive to the change in viscosity. Therefore, the speed measurement with wild type cells in non-Newtonian solutions also include the change in bundling process due to varied viscosity and non-Newtonian behaviors which potentially leads to a biased result.

In this study, in search for better understanding on how non-Newnotian effects change bacteria swimming speed, a smooth swimming *E.coli* strain, which has no tumble behavior, is used to quantify the swimming speed changes with respect to polymer concentrations. In addition, a wild type strain is tested to explain the non-Newtonian effects on flagellar bundling process. A three-dimensional tracking technique [33] is used in analyzing the swimming behavior. It is found the swimming speed is significantly enhanced and we believe this is due to shear-thinning effect. Plus the shear-induced normal stress plays an important role in forcing the cell to swim straighter [32] and reducing the bundling time.

5.2 Materials and methods

5.2.1 Cell preparation

The cells used in the experiments were smooth swimming *E.coli* (Strain: K12 HCB1736) and wild type *E.coli* (Strain: K12 AW405). The wild type cell is known to have a "run and tumble" motility [7] while the smooth swimming cell does not tumble. The culturing procedures for both strains are identical. A single colony was picked from agar plate and cultured in 10 ml T-Broth (1 L of water, 10 g of tryptone and 5 g of NaCl) by rotating at 200 rpm (Southwest Science, Incu-Shaker Mini) for 16 h at 30°C. 20 μl of bacteria suspension was cultured again in 10 ml of T-Broth for 4 h until mid-exponential growing phase of *E.coli*. The bacterial suspension was washed three times by centrifuging at 2000 rpm (Eppendorf, MiniSpin Plus) for 8 minutes and re-suspending in fresh motility buffer (1 L of water, 11.2 g K2HPO4, 4.8 g KH2PO4, 0.029 g EDTA, 3.9 g NaCl; pH 7-7.5). The final suspension was diluted three-fold before conducting experiments.

5.2.2 Polymer solutions

Ficoll 400 and Methocel 90 HG were prepared in this experiment as Newtonian and non-Newtonian polymer solutions. A 15% (wt/vol) stock solution of Ficoll 400 (Sigma-Aldrich) and a 0.5% (wt/vol) stock solution of Methocel 90 HG (Sigma-Aldrich) was prepared by dissolving the polymer in deionized water and rotating overnight at 200 rpm (Southwest Science, Incu-Shaker Mini). The polymer solution was dialyzed for 1 wk (Spectra/Por 2 Dialysis Trial Kit; 1214 kD MWCO, 23 mm flat-width membrane). The final polymer concentration was calculated by measuring

the weight before and after evaporating the solvent for 6 h at 60°C and placing the solution for 4 h in vacuum until the final weight reaches a constant.

5.2.3 Shear viscosity measurement

The shear viscosity of the solutions was measured using a rheometer (TA Instruments, AR2000) at different shear rates, ranging from 500 s^{-1} to 20000 s^{-1}, using 40 mm, 0.5° cone.

5.2.4 Text fixture

The cell motion was observed by placing a small volume of the cell suspension into a test fixture consisting of a swimming pool cut from a 1.5-mm film of polydimethylsiloxane (PDMS) and sandwiched between a No. 1 glass slide and a No. 1.5 glass cover slide.

5.2.5 Real-time 3D digital tracking microscopy

A 3D digital tracking microscope was used to observe the swimming behavior of the cells. The cells were observed using a Nikon TE200 inverted microscope with a CFI Plan Fluor20XMI objective and PCO edge 5.5 sCMOS camera. A 2D translational stage (Prior) was used for tracking the cells in the 2D plane parallel to the glass slide. A piezo objective positioner (Physik Instrumente, PI P-725.4CL) was used to rapidly control the position of the focal plane in real time so that the cell always remains in the field of view. Images were acquired at 80 fps with a resolution

of 320 pixels × 240 pixels. A real-time algorithm, written in C++ and OpenCV detected the position (centroid) of a single cell in the image and moved the stage and objective to maintained the cell in focus and within the field of view.

5.2.6 Modified Resistive Force Theory for wobbling cells

Our approach follows Darnton *et al.* [49]. For the force and torque on cell body we have

$$\begin{bmatrix} F_b \\ \tau_b \end{bmatrix} = \begin{bmatrix} A_b & 0 \\ 0 & D_b \end{bmatrix} \begin{bmatrix} v \\ \omega_b \end{bmatrix} \tag{5.1}$$

and for the flagellum we have

$$\begin{bmatrix} F_f \\ \tau_f \end{bmatrix} = \begin{bmatrix} A_f & B_f \\ Bf & D_f \end{bmatrix} \begin{bmatrix} v \\ \omega_f \end{bmatrix}, \tag{5.2}$$

where F_b, F_f and τ_b, τ_f are the force and torque on the cell body and flagellum, v is the swimming speed of the cell. ω_b and ω_f are the rotation rate of the cell body and flagellum respectively. The modification due to wobbling with an angle ϕ is to change the calculation of the drag coefficient of cell body. We assume that the cell body is a spheroid with length $2a$ and width $2b$, then A_b is given as

$$A_b = -(A_1 sin^2(\phi) + A_2 cos^2(\phi)) \tag{5.3}$$

and

$$D_b = -((D_1 + a^2 A_1) sin^2(\phi) + D_2 cos^2(\phi)). \tag{5.4}$$

For given viscosity μ, eccentricity $e = (a^2 - b^2)^{1/2}/a$, and $E = log[(1+e)/1-e]$, the values of the coefficients are

$$A_1 = 32\pi\mu a e^3/[(3e^2-1)E + 2e], \tag{5.5}$$

$$A_2 = 16\pi\mu a e^3(\phi)/[(1+e^2)E - 2e], \tag{5.6}$$

$$D_1 = 32\pi\mu a b^2 e^3(2-e^2)/3(1-e^2)[(1+e^2)E - 2e] \tag{5.7}$$

and

$$D_2 = 32\pi\mu a b^2 e^3/3[2e - (1-e^2)E]. \tag{5.8}$$

The resistance matrix for the flagellum in Equation 5.2 is a result of standard Resistive Force Theory (RFT) [58, 68, 69]:

$$A_f = \frac{2\pi\mu L \times (8\pi^2 R^2 + p^2)}{[log(\frac{r}{p}) + \frac{1}{2}][4\pi^2 R^2 + p^2]}, \tag{5.9}$$

$$B_f = \frac{2\pi\mu L \times (-2\pi R^2 p)}{[log(\frac{r}{p}) + \frac{1}{2}][4\pi^2 R^2 + p^2]} \tag{5.10}$$

and

$$D_f = \frac{2\pi\mu L \times (4\pi R^2 + 2p^2) r^2}{[log(\frac{r}{p}) + \frac{1}{2}][4\pi^2 R^2 + p^2]}\ , \tag{5.11}$$

where L is the length of the flagellar filament, p is the pitch the helix, R and r are the radius of the helix and filament respectively. The geometry of the cell body and flagellum used in our calculations is given in Table 5.1.

Table 5.1: Geometric parameters used in cell swimming calculations.

Symbol	Value
a	2.00 μm
b	0.60 μm
L	8.00 μm
p	2.00 μm
R	0.35 μm
r	0.03 μm

The coupled system is force free and torque free [5]:

$$F_f + F_b = 0 \tag{5.12}$$

and

$$\tau_f + \tau_b = 0 \ . \tag{5.13}$$

5.2.7 Quantify average curvature of 3D swimming trajectory

Since the tracking microscope records the cell motion at a slighly out-of-focus position, we were unable to directly measure the cell body wobbling [32]. Instead, we use the curvature of the swimming trajectory to quantify the overall wobbling effect. By definition, for any given object moving in a 3D space, the position of the object can be simply described as $\boldsymbol{r}(t)$. The curvature, $\kappa(t)$, is defined as

$$\kappa(t) = \frac{\left|\boldsymbol{r}'(t) \times \boldsymbol{r}''(t)\right|}{\left|\boldsymbol{r}'(t)\right|^3}. \tag{5.14}$$

To calculate the curvature from the cell trajectory in motility buffer, we choose the first 7 data points $r_i(t_j)$ ($i = 1, 2, 3$ and $j = 1 \sim 7$) and fit with a third order polynomial. The first and second order derivative of $\boldsymbol{r}(t)$ is evaluated from the fitted polynomial, and a local curvature $\kappa(t = t_1)$ is calculated using Equation 5.14. Then

a moving window with a time step $\delta t = 1/80$, where 80 is the frame rate used in the experiment, is applied and in this way the local curvature at different time (location) is estimated. Averaging over all time gives an measure of the trajectory curvature. For the trajectory in polymer solutions, the number of data points (j) for local curvature estimation was chosen depending on the average swimming speed. More data points were chosen for slower swimming cells so as to ensure a similar length was used for estimating local curvature. The number of time intervals ($j-1$) were chosen to be inversely proportional to the average swimming speed.

5.3 Results and discussion

5.3.1 Characterizing smooth swimming bacteria motility in Newtonian solutions

Starting with characterization of the smooth swimmer flagellar motor behavior, 25 individual cells were tracked in dialyzed Ficoll 400 solutions at various concentrations (viscosities) and the average swimming speed is shown in Fig. 5.2. The mean swimming speed decreases as the solution viscosity rises and, although the decline is monotonic throughout the range of viscosities tested, there is a clear change in the rate at which the speed declines for $\mu \sim> 5$ cP. The mean swimming speed decreases faster at higher viscosity and the decreasing rate scales on the order of $1/\mu$ (Fig. 5.2 dashed curve), suggesting that in this regime, the torque of the motor is constant. This has been previously observed experimentally [33, 65] and explained analytically [33, 58]. The swimming speed behavior at lower viscosities implies that the torque of the motor is increasing with respect to its rotational speed [33, 65].

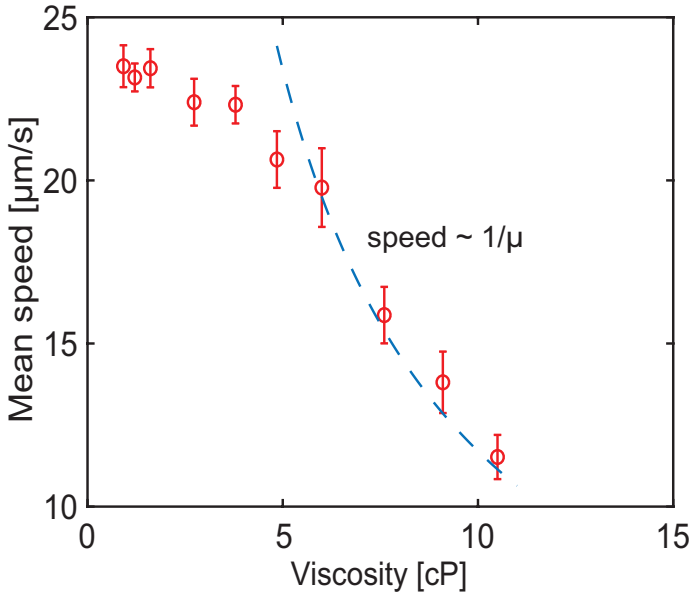

Figure 5.2: Mean swimming speed of smooth swimmers in dialyzed Ficoll 400 solutions. The red markers are the experimental data and the blue dashed curve shows that the mean speed decreases linearly as a function of viscosity indicating that the torque of the flagellar motor is constant.

The torque of the motor is estimated using Resistive Force Theory (RFT), described in detail earlier [33, 58] and shown in Fig. 5.3. The results are consistent with previous measurements of the flagella motor torque-speed characteristics [33, 49, 65, 66], although the knee speed of the motor is a little slower and the stall torque is a little larger than the one found in previous observation of wild type cells [33]. Nevertheless, the deviation may be due to genetic difference and the motor behavior still lies in a reasonable range compared with previous observations.

5.3.2 Shear-induced normal force reduces wobbling effect

Patteson *et al.* [32] measured the averaged wobbling angle and discovered that it decreased with respect to the rise of polymer concentration (viscosity). They also qualitatively demonstrated that the swimming trajectory were straighter and smoother in non-Newtonian solutions compared to Newtonian case. To compare

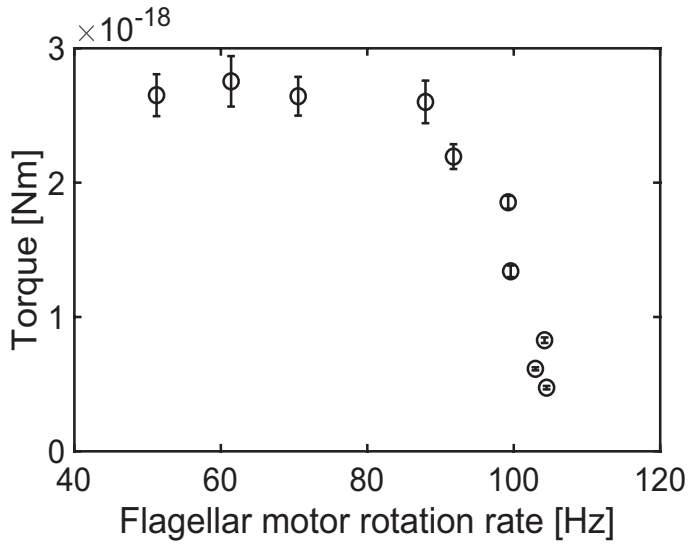

Figure 5.3: Smooth swimmer's flagellar motor torque behavior. The knee speed of the motor is about 100 Hz which is a bit smaller than the wild type cells [33, 65].

our results with Patteson *et al.*'s observation, the change in curvature as a function of viscosity is shown in Fig. 5.4, the averaged curvature of swimming trajectories in Newtonian solutions remains roughly constant with the viscosity increasing from 0.98 cP to 10.5 cP. Indicating that there is no significant change on wobbling angle in Newtonian solutions at varying viscosities.

However, in contrast, the averaged trajectory curvature in the Methocel soutions decreases as the fluid viscosity increases in the Methocel solutions. The reason for this change has been previously explained by Patteson *et al.* [32]. Shear-induced normal force, as one of the non-Newtonian effects in polymer solutions, has a significant impact on bacterial motility, especially the smoothness of their swimming trajectory. The rotational shear flow generated by the swimming behavior leads to a normal force pointing inwards the center-line of the cell as demonstrated in Fig. 5.1, forcing the cell to reduce its wobbling behavior.

The curvature of the trajectory calculated in this experiment shows that the trajectory indeed becomes straighter, as reflected by the decrease in averaged curvature,

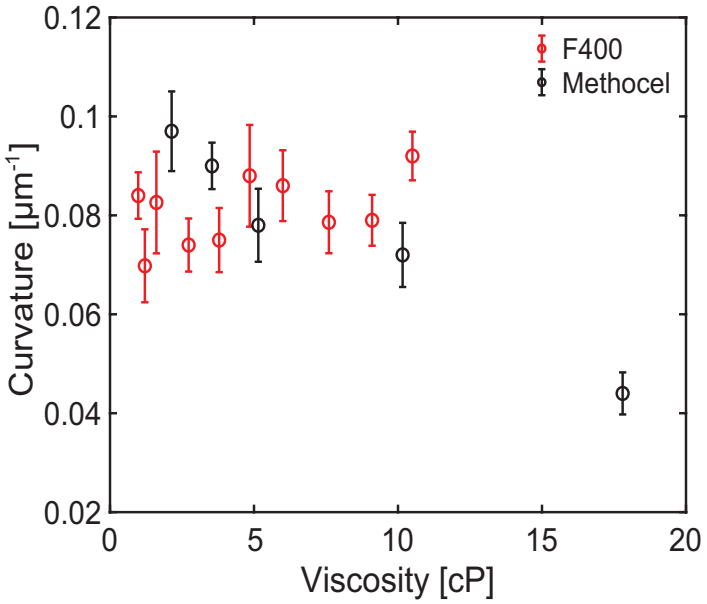

Figure 5.4: Averaged local curvature of all swimming trajectories at different viscosities. Red markers show the results in dialyzed Ficoll 400 solutions and black markers are the results in dialyzed Methocel solutions.

which agrees well with Patteson *et al.*'s results.

5.3.3 Shear-thinning enhances bacteria swimming speed

The same experiment is repeated, again using smooth-swimmer cells, in Methocel solutions which is known to be non-Newtonian [24,32], exhibiting both shear-thinning [119] and viscoelastic behavior [32, 120]. The first notable result of swimming in non-Newtonian fluids is the change in the mean swimming speed. Compared to the decreasing trend of the mean swimming speed that was observed in the case of the Newtonian solution, the mean swimming speed in non-Newtonian solutions increases quite significantly as a function of shear viscosity (Fig. 5.5, black markers).

This enhanced motilility was also observed by Patteson *et al.* [32] who argued that one important contribution to the rise in swimming speed was the shear-induced

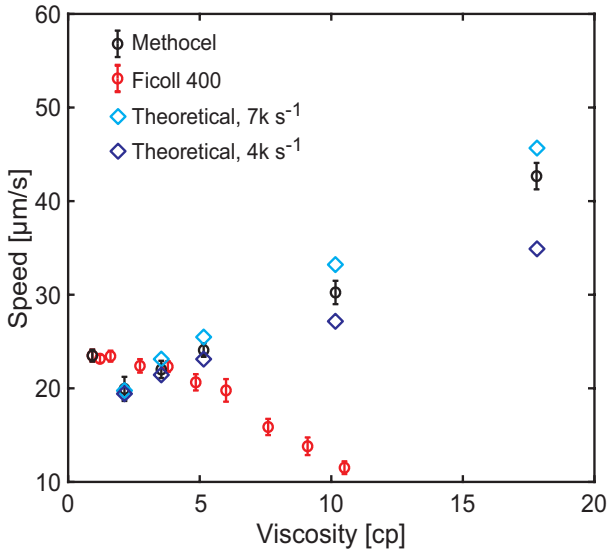

Figure 5.5: Mean swimming speed of smooth swimmers in Ficoll 400 (red) and Methocel solutions (black). The viscosity is the shear viscosity measured at 200 s^{-1}. The swimming speed decreases with increased viscosity in Ficoll 400 solutions, while increases with increased viscosity in Methocel solutions. Shear-thinning effect is proposed to explain the speed enhancement and estimated swimming speed in Methocel solution using shear-dependent RFT model [34] is plotted in light and dark blue markers, which are calculated assuming $\dot{\gamma}_f = 7000\ s^{-1}$ and $\dot{\gamma}_f = 4000\ s^{-1}$ respectively.

normal force, which plays a significant role in forcing the cell to swim along a less "wobbly" path. *E.coli* cells are known to wobble [49, 116] during swimming and shear-induced normal force reduces the wobbling angle which could potentially enhance the swimming efficiency. However, we believe such enhancement, if present, represents a subtle effect. To estimate the effect of cell body precession on swimming speed, a modified RFT, given by Darton *et al.* [49], is used to estimate the swimming speed with different wobbling angle ϕ. A larger ϕ leads to a higher drag coefficient on cell body and lower swimming speed. Assuming a constant torque motor, the calculated swimming speed increases about 10 % with ϕ goes from $\pi/2$ to 0 (Fig. 5.6). Furthermore, it is not clear that the cell precession reduces swimming speed, and Liu *et al.* argued that such motion may, under some conditions, enhance the swimming efficiency of bacteria [19, 121]. In both cases, the Resistive Force Theory predicts modest changes in swimming speed while the present data indicate as much as a three-fold increase in the swimming speed over the speed achieved in the Newto-

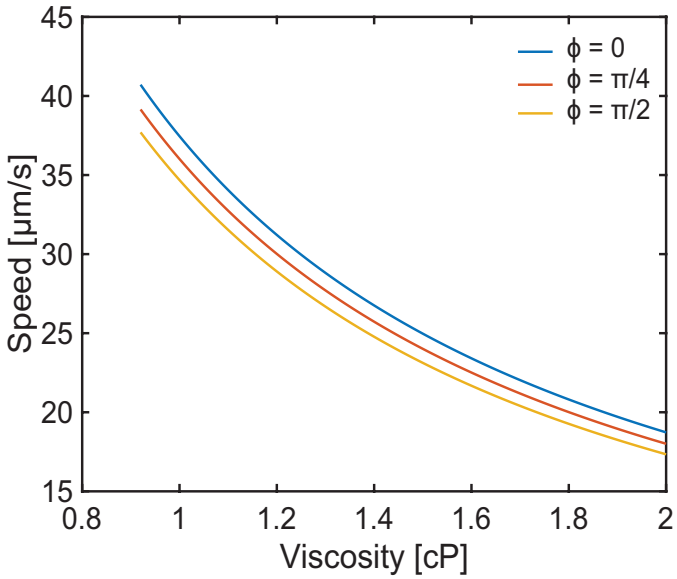

Figure 5.6: Estimated swimming speed of bacteria *E.coli* with different precession angles ϕ using modified RFT [49].

nian solution with the equivalent shear viscosity (Fig. 5.5). For these reasons, we argue that cell precession is insufficient to explain the speed enhancement observed (Fig. 5.5) in this experiment purely by the shear-induced normal force.

Elasticity of polymer solutions has also been claimed [54, 55] to potentially enhance the speed of helical swimmers within a certain range of De numbers, where De number is defined as $De = \omega_f \tau$. However, the results from both Spagnolie *et al.*'s numerical study [55] and Liu *et al.*'s [54] experimental results show that the largest increase in swimming speed is less than 20% compared to the speed in Newtonian solution with same viscosity. Again, the significant speed enhancement observed in this experiment seems to be too high to be explained by viscoelastic behavior of the Methocel medium.

What could be the reason for such significant speed enhancement? Magariyama and Kudo first proposed that an anisotropic viscosity (different viscosity on tangential and normal direction) experienced by the swimmer lead to an enhancement in

swimming speed [58]. More recently, shear-thinning has been proposed to explain the speed increase of flagellated bacteria swimming in polymer solutions [34, 118, 122]. From the previous result [33, 58], it is noticed that the cell body rotation rate ω_c is smaller than the flagella rotation rate ω_f. The shear rate $\dot{\gamma}$ near the flagella, which is estimated as $\dot{\gamma}_f = \omega_f R/r_0$ [34], where R and r_0 are the radius of flagellar bundle and filament respectively, reaches as high as $10^4\ s^{-1}$. In contrast, due to the lower rotation rate and the larger cell body radius, the shear rate near cell body remains quite low: $\dot{\gamma}_c \sim 10^2\ s^{-1}$. If the polymer solution is shear thinning, then the viscosity experienced by the flagella could be much smaller than the viscosity experienced by the cell body.

A cone-and-plate rheometer (TA instrument, AR 2000) was used to measure the shear rheology of both Methocel and Ficoll solutions. The shear dependent viscosity, shown in Fig. 5.7, demonstrates that Methocel solution has a strong shear-thinning effect at high concentration, while the viscosity of Ficoll solution is nearly shear independent. A non-linear curve fitting using a power-law model [28] $\mu = m\dot{\gamma}^{n-1}$ is applied on the shear viscosity of Methocel solutions. For Newtonian solutions, the power law index n is 1, while for Methocel solutions the shear-thinning index ranges from 0.989 to 0.736, and is given in Table 5.2.

Table 5.2: Consistency index and exponent of Methocel solutions using power-law model.

Concentration [%]	0.500	0.375	0.250	0.188	0.125	0.063
m	0.103	0.034	0.009	0.005	0.003	0.001
n	0.736	0.803	0.885	0.923	0.955	0.989

Using the modified shear-thinning RFT proposed by Martinez *et al.* [34], the motility matrices Equation 5.1 and Equation 5.2 are recalculated assuming two shear rates, $\dot{\gamma}_f = 7000\ s^{-1}$ and $\dot{\gamma}_f = 4000\ s^{-1}$ near flagella, while the viscosity near cell body is the polymer solution bulk viscosity measured at $200\ s^{-1}$. The speed of smooth swimming *E.coli* is then estimated using the modified shear-thinning RFT

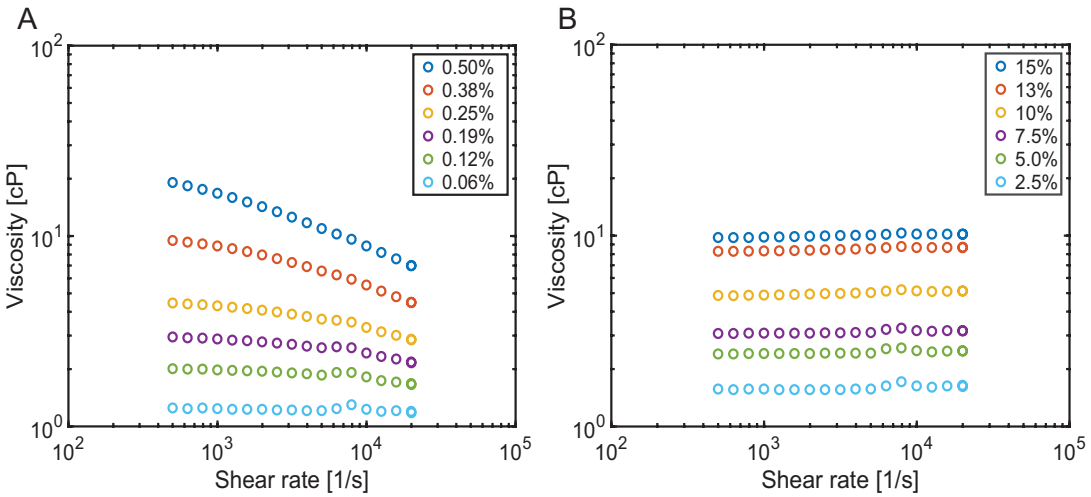

Figure 5.7: Shear viscosity of polymer solutions. A, Methocel solutions. B, Ficoll solutions.

and the motor behavior computed from the Newtonian case. The result (Fig. 5.5) shows a good agreement with the experimental observation.

5.3.4 Shear-induced normal force reduces flagellar bundling time

The flagellar bundling time is extended with an increased viscosity in Newtonian solutions [33]. It is equally interesting to observe how non-Newtonian effects change the flagellar bundling process. The skewness of individual speed distribution has been previously stated [33] to be a good characteristic number to quantify bundling time. And an increased skewness indicates a longer bundling time.

The same experiment [33] in Methocel solutions is done using wild type *E.coli* (K12 AW405). Using similar process for data analysis [33], the average skewness of individual speed distribution of cells swimming in non-Newtonian solutions shows a different trend with respect to varying viscosity (Fig. 5.8). Skewness increases initially and then decays at higher viscosity, suggesting that the bundling time is

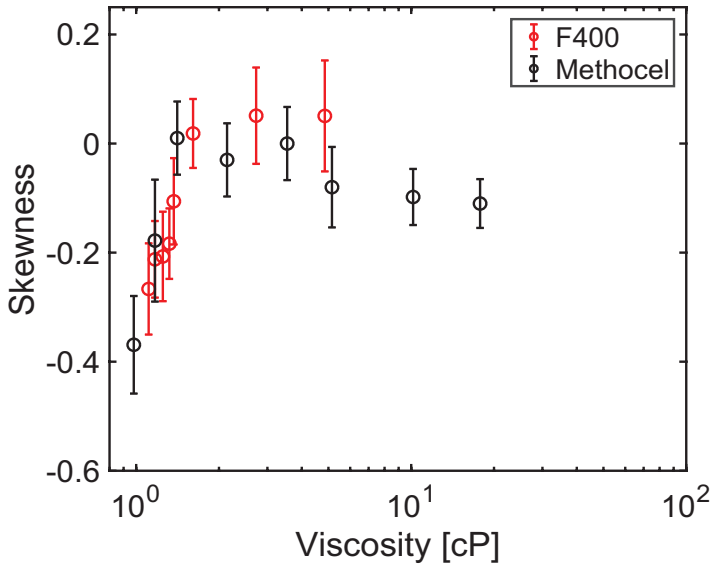

Figure 5.8: Averaged skewness of speed distribution as a function of viscosity. Skewness increases with respect to viscosity in Newtonian case (F400 dialzyed), indicating an extended bundling time. Skewness increases initially with respect to viscosity then decays in non-Newtonian case (Methocel dialyzed).

shorter at higher viscosity.

Understanding the mechanics during bundling process is necessary to explain such phenomenon. It has been experimentally tested and shown that the bundling process is a pure hydrodynamic process [26] in Newtonian solutions. More recently, Man *et al.* [123] estimated the hydrodynamic interactions among rotating elastic slender rods that were closely located and revealed the force balance during bundling process. In Newtonian solutions, the hydrodynamic interactions are balanced by the viscous drag and bending rigidity (elastic force) of the flagellar filaments. Since we remain in the low Reynolds number regime [123], the force balance on each filament is written instantaneously as

$$f_e + f_h + f_v = 0, \tag{5.15}$$

where f_e, f_h and f_v refer respectively to elastic, hydrodynamic and viscous force on the filament. Two dimensionless numbers are used to describe the relations between

these three forces. Sperm number, Sp, quantifying the a balance between viscous drag and elastic force, is defined as

$$SP = (\frac{\xi_\perp \omega_f L^4}{A})^{1/4}, \tag{5.16}$$

where $\xi_\perp$ is the viscous drag coefficient of a slender body on perpendicular direction [23] defined as

$$\xi_\perp = \frac{4\pi\mu}{log(L/r_0)} \tag{5.17}$$

and A is the bending modulus of the filaments [124]. Bundling number, Bu, which compares the driving force in the bundling process to the viscous force [123] is defined as

$$Bu = \frac{r_0^2 Sp^4}{b^2}, \tag{5.18}$$

where r_0 and b are the geometry of the system given in Fig. 5.9. The range of Bu number (with $\omega_f \sim 100$ Hz) lies in $0.1 \sim 1$ indicating a force balance during bundling process.

In Fig. 5.1 and Fig. 5.4, shear-induced normal force has been shown to play a significant role in forcing the cell to swim straighter. Here, we suspect the reduced bundling time is also due to shear-induced normal force acting on the flagellar filaments. For bundling in non-Newtonian system, the force balance is rewritten as

$$f_e + f_h + f_v + f_n = 0, \tag{5.19}$$

where f_n is the shear-induced normal force. We estimate the shear-induced normal force on same configuration shown in Fig. 5.9, a rotating rod. In the previous chapter, we have shown that Methocel solutions indeed have viscoelastic behavior with a single relaxation time. Therefore, an Oldroyd-B model [112] is assumed to analyze

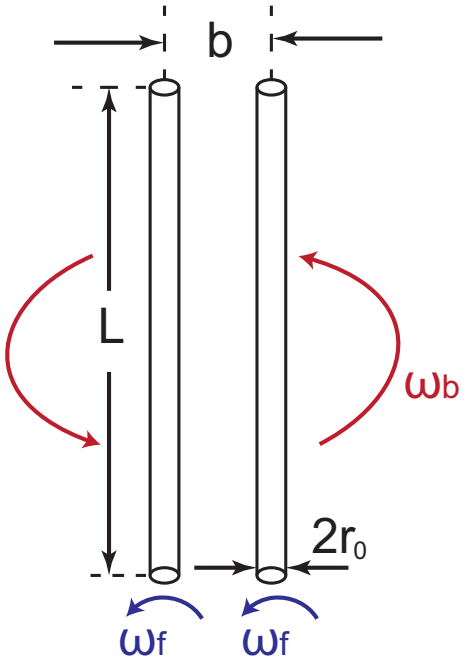

Figure 5.9: Schematic of two flagellar filaments in analytical model. ω_f is the rotation rate of the filaments and ω_b is the angular velocity of the filament along the bundle centerline.

this problem. Let the filament rotate at ω_f and is contained by a fixed cylindrical container of radius R_0. Assuming the form of the fluid velocity

$$\mathbf{u} = v(r)\hat{\boldsymbol{\theta}}, \tag{5.20}$$

the rate of strain tensor is then given by

$$A = (\frac{\partial v}{\partial r} - \frac{v}{r})(\hat{\boldsymbol{\theta}}\hat{\boldsymbol{r}} + \hat{\boldsymbol{r}}\hat{\boldsymbol{\theta}}). \tag{5.21}$$

The total viscosity of the solution is written as $\mu = \mu_s + \mu_p$ [125] where μ_s and μ_p are the solvent viscosity and polymer viscosity respectively. The stress tensor S in polymer solutions can be written as

$$S = \mu_S A + S_p, \tag{5.22}$$

where S_p is the stress due to polymer contribution. Inserting it into the governing equation of an Oldroyd-B model [112]

$$S + \tau \overset{\nabla}{S} = \mu(A + \frac{\mu_s}{\mu}\tau \overset{\nabla}{A}), \tag{5.23}$$

plus the momentum balance equation

$$\nabla p = \nabla \cdot S \tag{5.24}$$

and continuity equation

$$\nabla \cdot \boldsymbol{u} = 0. \tag{5.25}$$

It is shown that

$$v(r) = r_0^2 \omega_f \frac{R_0^2 - r^2}{r(R_0^2 - r_0^2)} \tag{5.26}$$

and

$$p = 2\mu\tau(1 - \frac{\mu_s}{\mu})\omega_f^2 \frac{r_0^4 R_0^4}{r^4(R_0^2 - r_0^2)^2}. \tag{5.27}$$

The torque per unit length is then given by

$$\int_0^{2\pi} r_0 S_{r\theta} d\theta = -4\pi\mu r_0 \omega_f \tag{5.28}$$

and the shear-induced normal stress is given by

$$f_n = 2\mu\tau(\frac{\mu_s}{\mu} - 1)\omega_f^2 \frac{R_0^4}{(R_0^2 - r_0^2)^2}\hat{\boldsymbol{r}}. \tag{5.29}$$

In the case of $R_0 \to \infty$, this normal stress f_n is written as

$$f_n = 2\tau(\mu_s - \mu)\omega_f^2 \hat{\boldsymbol{r}}. \tag{5.30}$$

It is noticed that the shear-induced normal force acts like a strangulation on the filament, and the word strangulation was mentioned by Saverio Spagnolie during his discussion with the authors. Thus, we define a dimensionless number, strangulation number (Str), comparing the shear-induced normal force to the viscous force during bundling process

$$Str = \frac{2\tau(\mu - \mu_s)\omega_f^2(2\pi r_0)}{\xi_\perp \omega_f b} = \frac{2\tau(\mu - \mu_s)\omega_f(2\pi r_0)}{\xi_\perp b} = \frac{2De(\mu - \mu_s)(2\pi r_0)}{\xi_\perp b}. \quad (5.31)$$

The Str number estimated using Equation 5.31 ($\tau \sim 1$ - 10 ms as given in Chapter 4) in this experiment is $0.03 \sim 0.3$, showing that the shear-induced normal force is about one third of the hydrodynamics force in helping the bundling process which is the reason for the reduced bundling time reflected by the change in skewness (Fig. 5.8).

5.4 Summary and Conclusions

We have shown that the motility of smooth swimming *E.coli* is significantly affected by the non-Newtonian behavior in polymer solutions. The averaged speed is enhanced with the presence of long chain polymer. Although effect of shear-induced normal force [32] and viscoelasticity [55] potentially increase the swimming speed, we believe the shear-thinning behavior is the key factor for the huge speed enhancement we observed in this study. Shear-induced normal force does contribute to the bundling process of a wild type *E.coli* cell, in assisting the hydrodynamic interactions among filaments and reducing the bundling time.

We believe that a better understanding of swimming in non-Newtonian solutions

has been produced from this study. Further experiments, simulations, especially visualizing the flagellar filaments [14,48] are necessary in understanding the bundling process in non-Newtonian solutions. Experiments using scaled artificial swimmers [118,126] in solutions that is either shear-thinning or viscoelastic will provide further evidence in order to define the non-Newtonian effects on bacteria swimming speed.

Chapter Six

Conclusion

A special experimental technique is documented in the first part of the thesis. Although the three-dimensional real-time tracking microscopy was originally developed by Berg and Brown back in 1972 [7]. This technique has not been redeveloped by other researchers until recently [19], plus it is not widely used partly due to the difficulties on real-time image processing and the design of feedback control system. However, we have shown that three-dimensional real-time tracking microscopy is a very useful technique in providing unique perspective on microorganism swimming problems. The system can be further developed and improved on both the software and hardware parts.

The main problem that is investigated in this thesis is on bacteria swimming in polymer solutions. With the three-dimensional real-time tracking microscope, we start with repeating the same experiment done by Berg and Brown [7] and Molaei *et al.* [37] to observe the "run and tumble" behavior of wild type *E.coli* in motility buffer. Similar results are reproduced [33] and we naturally extend the study on bacterial motility in Newtonian polymer solutions with varying viscosities. It is discovered that not only the swimming speed is affected by the change in viscosity but also the bundling duration, which is characterized by the change in individual speed skewness.

In later part of the thesis, we characterize the viscoelastic behavior of long chain polymer solutions using microrheology method. We propose the use of standard fluorescent microscopy and SPT method in replacement of classical measurement techniques such as DLS. With the ability to resolve the viscoelastic modulus at high frequency, our method is easier to implement at lower cost.

Finally, we explore how non-Newtonian effects change bacteria motility. Shear-thinning effect is observed to enhance the swimming speed significantly due to the

different viscosity experienced by the cell body and flagella respectively. Shear-induced normal force plays an important role in reducing the bundling duration and we quantitatively compare this force with viscous drag during bundling process using a theoretical model.

Although characterizing the flagella bundling time using individual speed skewness is promising, a direct measurement on bundling time with flagellum visualization during bundling process is necessary to further extend and complete this study. In the second project, the method is still limited in resolving high frequency viscoealstic behavior. Plus the image processing algorithm can be improved to reduce the cost. Lastly, it is hard to separate different non-Newtonian factors (shear-thinning, viscoelastic and shear-induced normal force) in analyzing the their effects on bacteria motility. Future measurements using artificial swimmers, simulations and theoretical works should aim to solve individual non-Newtonian effects on flagellated bacteria motility.

Bibliography

[1] M. Sfakiotakis, D. M. Lane, and J. B. C. Davies, "Review of fish swimming modes for aquatic locomotion," *IEEE Journal of oceanic engineering*, vol. 24, no. 2, pp. 237–252, 1999.

[2] J. O. Dabiri, M. Gharib, S. P. Colin, and J. H. Costello, "Vortex motion in the ocean: in situ visualization of jellyfish swimming and feeding flows," *Physics of Fluids*, vol. 17, no. 9, p. 091108, 2005.

[3] O. Reynolds, "Xxix. an experimental investigation of the circumstances which determine whether the motion of water shall he direct or sinuous, and of the law of resistance in parallel channels," *Philosophical Transactions of the Royal Society of London*, vol. 174, pp. 935–982, 1883.

[4] F. E. Fish, "Comparative kinematics and hydrodynamics of odontocete cetaceans: morphological and ecological correlates with swimming performance.," *Journal of Experimental Biology*, vol. 201, no. 20, pp. 2867–2877, 1998.

[5] E. M. Purcell, "Life at low Reynolds number," *Am. J. Phys*, vol. 45, no. 1, pp. 3–11, 1977.

[6] S. Kim and S. J. Karrila, *Microhydrodynamics: principles and selected applications*. Courier Corporation, 2013.

[7] H. C. Berg and D. A. Brown, "Chemotaxis in *Escherichia coli* analysed by three-dimensional tracking," *Nature*, vol. 239, no. 5374, pp. 500–504, 1972.

[8] H. C. Berg, *E. coli in Motion*. Springer Science & Business Media, 2008.

[9] A. Terray, J. Oakey, and D. W. Marr, "Microfluidic control using colloidal devices," *Science*, vol. 296, no. 5574, pp. 1841–1844, 2002.

[10] M. J. Kim and K. S. Breuer, "Enhanced diffusion due to motile bacteria," *Physics of fluids*, vol. 16, no. 9, pp. L78–L81, 2004.

[11] P. Nelson, *Biological physics*. WH Freeman New York, 2004.

[12] J. S. Guasto, R. Rusconi, and R. Stocker, "Fluid mechanics of planktonic microorganisms," *Annual Review of Fluid Mechanics*, vol. 44, pp. 373–400, 2012.

[13] B. Qin, A. Gopinath, J. Yang, J. P. Gollub, and P. E. Arratia, "Flagellar kinematics and swimming of algal cells in viscoelastic fluids," *Scientific reports*, vol. 5, p. 9190, 2015.

[14] L. Turner, W. S. Ryu, and H. C. Berg, "Real-time imaging of fluorescent flagellar filaments," *Journal of bacteriology*, vol. 182, no. 10, pp. 2793–2801, 2000.

[15] J. Gray and G. Hancock, "The propulsion of sea-urchin spermatozoa," *Journal of Experimental Biology*, vol. 32, no. 4, pp. 802–814, 1955.

[16] D. Bray, *Cell movements: from molecules to motility*. Garland Science, 2000.

[17] H. C. Berg, "How spiroplasma might swim," *Journal of bacteriology*, vol. 184, no. 8, pp. 2063–2064, 2002.

[18] J. E. Avron and O. Raz, "A geometric theory of swimming: Purcell's swimmer and its symmetrized cousin," *New Journal of Physics*, vol. 10, no. 6, p. 063016, 2008.

[19] B. Liu, M. Gulino, M. Morse, J. X. Tang, T. R. Powers, and K. S. Breuer, "Helical motion of the cell body enhances caulobacter crescentus motility," *Proceedings of the National Academy of Sciences*, vol. 111, no. 31, pp. 11252–11256, 2014.

[20] R. P. McCord, J. N. Yukich, and K. K. Bernd, "Analysis of force generation during flagellar assembly through optical trapping of free-swimming *Chlamydomonas reinhardtii*," *Cytoskeleton*, vol. 61, no. 3, pp. 137–144, 2005.

[21] K. König, L. Svaasand, Y. Liu, G. Sonek, P. Patrizio, Y. Tadir, M. Berns, and B. Tromberg, "Determination of motility forces of human spermatozoa using an 800 nm optical trap.," *Cellular and molecular biology (Noisy-le-Grand, France)*, vol. 42, no. 4, pp. 501–509, 1996.

[22] E. Lauga and T. R. Powers, "The hydrodynamics of swimming microorganisms," *Reports on Progress in Physics*, vol. 72, no. 9, p. 096601, 2009.

[23] J. Lighthill, "Flagellar hydrodynamics," *SIAM review*, vol. 18, no. 2, pp. 161–230, 1976.

[24] H. C. Berg and L. Turner, "Movement of microorganisms in viscous environments," *Nature*, vol. 278, no. 5702, pp. 349–351, 1979.

[25] H.-C. Ho and S. S. Suarez, "Hyperactivation of mammalian spermatozoa: function and regulation," *Reproduction*, vol. 122, no. 4, pp. 519–526, 2001.

[26] M. Kim, J. C. Bird, A. J. Van Parys, K. S. Breuer, and T. R. Powers, "A macroscopic scale model of bacterial flagellar bundling," *Proceedings of the National Academy of Sciences*, vol. 100, no. 26, pp. 15481–15485, 2003.

[27] R. L. Panton, *Incompressible flow*. Wiley Online Library, 1984.

[28] H. A. Barnes, J. F. Hutton, and K. Walters, *An introduction to rheology*, vol. 3. Elsevier, 1989.

[29] D. Roylance, "Engineering viscoelasticity," *Department of Materials Science and Engineering–Massachusetts Institute of Technology, Cambridge MA*, vol. 2139, pp. 1–37, 2001.

[30] T. Dalton, S. E. Dowd, R. D. Wolcott, Y. Sun, C. Watters, J. A. Griswold, and K. P. Rumbaugh, "An in vivo polymicrobial biofilm wound infection model to study interspecies interactions," *PloS one*, vol. 6, no. 11, p. e27317, 2011.

[31] D. L. Valentine, J. D. Kessler, M. C. Redmond, S. D. Mendes, M. B. Heintz, C. Farwell, L. Hu, F. S. Kinnaman, S. Yvon-Lewis, M. Du, *et al.*, "Propane respiration jump-starts microbial response to a deep oil spill," *Science*, vol. 330, no. 6001, pp. 208–211, 2010.

[32] A. Patteson, A. Gopinath, M. Goulian, and P. Arratia, "Running and tumbling with *E. coli* in polymeric solutions," *Scientific reports*, vol. 5, 2015.

[33] Z. Qu, F. Z. Temel, R. Henderikx, and K. S. Breuer, "Changes in the flagellar bundling time account for variations in swimming behavior of flagellated bacteria in viscous media," *Proceedings of the National Academy of Sciences*, p. 201714187, 2018.

[34] V. A. Martinez, J. Schwarz-Linek, M. Reufer, L. G. Wilson, A. N. Morozov, and W. C. Poon, "Flagellated bacterial motility in polymer solutions," *Proceedings of the National Academy of Sciences*, vol. 111, no. 50, pp. 17771–17776, 2014.

[35] P. R. Smith, I. E. Morrison, K. M. Wilson, N. Fernandez, and R. J. Cherry, "Anomalous diffusion of major histocompatibility complex class i molecules on hela cells determined by single particle tracking," *Biophysical Journal*, vol. 76, no. 6, pp. 3331–3344, 1999.

[36] V. Levi, Q. Ruan, and E. Gratton, "3-d particle tracking in a two-photon microscope: application to the study of molecular dynamics in cells," *Biophysical journal*, vol. 88, no. 4, pp. 2919–2928, 2005.

[37] M. Molaei, M. Barry, R. Stocker, and J. Sheng, "Failed escape: solid surfaces prevent tumbling of escherichia coli," *Physical review letters*, vol. 113, no. 6, p. 068103, 2014.

[38] J. S. Guasto, P. Huang, and K. S. Breuer, "Statistical particle tracking velocimetry using molecular and quantum dot tracer particles," *Experiments in fluids*, vol. 41, no. 6, pp. 869–880, 2006.

[39] Y. Pu, X. Song, and H. Meng, "Holographic piv for diagnosing particulate flows," *Exp. Fluids*, vol. 29, pp. 117–128, 2000.

[40] H. Cang, C. M. Wong, C. S. Xu, A. H. Rizvi, and H. Yang, "Confocal three dimensional tracking of a single nanoparticle with concurrent spectroscopic readouts," *Applied physics letters*, vol. 88, no. 22, p. 223901, 2006.

[41] A. D. Dinsmore, E. R. Weeks, V. Prasad, A. C. Levitt, and D. A. Weitz, "Three-dimensional confocal microscopy of colloids," *Applied optics*, vol. 40, no. 24, pp. 4152–4159, 2001.

[42] D. Zill, W. S. Wright, and M. R. Cullen, *Advanced engineering mathematics*. Jones & Bartlett Learning, 2011.

[43] H. Hotani, "Micro-video study of moving bacterial flagellar filaments: III. Cyclic transformation induced by mechanical force," *Journal of molecular biology*, vol. 156, no. 4, pp. 791–806, 1982.

[44] H. C. Berg and L. Turner, "Torque generated by the flagellar motor of *Escherichia coli*," *Biophysical journal*, vol. 65, no. 5, pp. 2201–2216, 1993.

[45] H. C. Berg and L. Turner, "Cells of *Escherichia coli* swim either end forward.," *Proceedings of the National Academy of Sciences*, vol. 92, no. 2, pp. 477–479, 1995.

[46] G. M. Fraser and C. Hughes, "Swarming motility," *Current opinion in microbiology*, vol. 2, no. 6, pp. 630–635, 1999.

[47] T. R. Powers, "Role of body rotation in bacterial flagellar bundling," *Physical Review E*, vol. 65, no. 4, p. 040903, 2002.

[48] L. Turner, L. Ping, M. Neubauer, and H. C. Berg, "Visualizing flagella while tracking bacteria," *Biophysical journal*, vol. 111, no. 3, pp. 630–639, 2016.

[49] N. C. Darnton, L. Turner, S. Rojevsky, and H. C. Berg, "On torque and tumbling in swimming *Escherichia coli*," *Journal of bacteriology*, vol. 189, no. 5, pp. 1756–1764, 2007.

[50] R. B. Kimsey and A. Spielman, "Motility of lyme disease spirochetes in fluids as viscous as the extracellular matrix," *Journal of Infectious Diseases*, vol. 162, no. 5, pp. 1205–1208, 1990.

[51] E. Lauga, "Propulsion in a viscoelastic fluid," *Physics of Fluids (1994-present)*, vol. 19, no. 8, p. 083104, 2007.

[52] H. C. Fu, T. R. Powers, and C. W. Wolgemuth, "Theory of swimming filaments in viscoelastic media," *Physical review letters*, vol. 99, no. 25, p. 258101, 2007.

[53] A. Leshansky, "Enhanced low-Reynolds-number propulsion in heterogeneous viscous environments," *Physical Review E*, vol. 80, no. 5, p. 051911, 2009.

[54] B. Liu, T. R. Powers, and K. S. Breuer, "Force-free swimming of a model helical flagellum in viscoelastic fluids," *Proceedings of the National Academy of Sciences*, vol. 108, no. 49, pp. 19516–19520, 2011.

[55] S. E. Spagnolie, B. Liu, and T. R. Powers, "Locomotion of helical bodies in viscoelastic fluids: enhanced swimming at large helical amplitudes," *Physical review letters*, vol. 111, no. 6, p. 068101, 2013.

[56] M. Dasgupta, B. Liu, H. C. Fu, M. Berhanu, K. S. Breuer, T. R. Powers, and A. Kudrolli, "Speed of a swimming sheet in newtonian and viscoelastic fluids," *Physical Review E*, vol. 87, no. 1, p. 013015, 2013.

[57] A. K. Balin, A. Zöttl, J. M. Yeomans, and T. N. Shendruk, "Biopolymer dynamics driven by helical flagella," *Phys. Rev. Fluids*, vol. 2, p. 113102, Nov 2017.

[58] Y. Magariyama and S. Kudo, "A mathematical explanation of an increase in bacterial swimming speed with viscosity in linear-polymer solutions," *Biophysical journal*, vol. 83, no. 2, pp. 733–739, 2002.

[59] K. A. Fahrner, W. S. Ryu, and H. C. Berg, "Biomechanics: bacterial flagellar switching under load," *Nature*, vol. 423, no. 6943, pp. 938–938, 2003.

[60] J. Yuan, K. A. Fahrner, and H. C. Berg, "Switching of the bacterial flagellar motor near zero load," *Journal of molecular biology*, vol. 390, no. 3, pp. 394–400, 2009.

[61] H. C. Berg, *Random walks in biology*. Princeton University Press, 1993.

[62] W. R. Schneider and R. Doetsch, "Effect of viscosity on bacterial motility," *Journal of Bacteriology*, vol. 117, no. 2, pp. 696–701, 1974.

[63] J. Schwarz-Linek, C. Valeriani, A. Cacciuto, M. Cates, D. Marenduzzo, A. Morozov, and W. Poon, "Phase separation and rotor self-assembly in active particle suspensions," *Proceedings of the National Academy of Sciences*, vol. 109, no. 11, pp. 4052–4057, 2012.

[64] R. Nossal, S.-H. Chen, and C.-C. Lai, "Use of laser scattering for quantitative determinations of bacterial motility," *Optics Communications*, vol. 4, no. 1, pp. 35–39, 1971.

[65] X. Chen and H. C. Berg, "Torque-speed relationship of the flagellar rotary motor of *Escherichia coli*," *Biophysical Journal*, vol. 78, no. 2, pp. 1036–1041, 2000.

[66] S. W. Reid, M. C. Leake, J. H. Chandler, C.-J. Lo, J. P. Armitage, and R. M. Berry, "The maximum number of torque-generating units in the flagellar motor of *Escherichia coli* is at least 11," *Proceedings of the National Academy of Sciences*, vol. 103, no. 21, pp. 8066–8071, 2006.

[67] J. Happel and H. Brenner, "Low Reynolds number hydrodynamics, noordhoff int," *Publishing, Leyden, Netherland*, vol. 235, 1973.

[68] M. Holwill and R. Burge, "A hydrodynamic study of the motility of flagellated bacteria," *Archives of biochemistry and biophysics*, vol. 101, no. 2, pp. 249–260, 1963.

[69] Y. Magariyama, S. Sugiyama, K. Muramoto, I. Kawagishi, Y. Imae, and S. Kudo, "Simultaneous measurement of bacterial flagellar rotation rate and swimming speed," *Biophysical journal*, vol. 69, no. 5, pp. 2154–2162, 1995.

[70] N. C. Darnton and H. C. Berg, "Force-extension measurements on bacterial flagella: triggering polymorphic transformations," *Biophysical journal*, vol. 92, no. 6, pp. 2230–2236, 2007.

[71] G. Volpe, I. Buttinoni, D. Vogt, H.-J. Kümmerer, and C. Bechinger, "Microswimmers in patterned environments," *Soft Matter*, vol. 7, no. 19, pp. 8810–8815, 2011.

[72] M. Garcia, S. Berti, P. Peyla, and S. Rafaï, "Random walk of a swimmer in a low-Reynolds-number medium," *Physical Review E*, vol. 83, no. 3, p. 035301, 2011.

[73] C. C. Miller, "The Stokes-Einstein law for diffusion in solution," *Proceedings of the Royal Society of London. Series A, Containing Papers of a Mathematical and Physical Character*, vol. 106, no. 740, pp. 724–749, 1924.

[74] C. D. Han, *Rheology in polymer processing*. Academic Press, 1976.

[75] M. Baumgärtel and N. Willenbacher, "The relaxation of concentrated polymer solutions," *Rheologica acta*, vol. 35, no. 2, pp. 168–185, 1996.

[76] R. B. Bird *et al.*, *Dynamics of polymeric liquids.-*. Wiley, 1977.

[77] R. D. Hester and D. Squire, "Rheology of waterborne coatings," *Journal of coatings technology*, vol. 69, no. 864, pp. 109–114, 1997.

[78] S.-i. Karato, Z. Wang, B. Liu, and K. Fujino, "Plastic deformation of garnets: systematics and implications for the rheology of the mantle transition zone," *Earth and Planetary Science Letters*, vol. 130, no. 1-4, pp. 13–30, 1995.

[79] A. Zettlemoyer and G. Lower, "The rheology of printing inks. iii. studies of simple dispersions," *Journal of Colloid Science*, vol. 10, no. 1, pp. 29–45, 1955.

[80] F. Amblard, B. Yurke, A. Pargellis, and S. Leibler, "A magnetic manipulator for studying local rheology and micromechanical properties of biological systems," *Review of Scientific Instruments*, vol. 67, no. 3, pp. 818–827, 1996.

[81] G. R. Cokelet, E. Merrill, E. Gilliland, H. Shin, A. Britten, and R. Wells Jr, "The rheology of human bloodmeasurement near and at zero shear rate," *Transactions of the Society of Rheology*, vol. 7, no. 1, pp. 303–317, 1963.

[82] J. D. Ferry, *Viscoelastic properties of polymers*. John Wiley & Sons, 1980.

[83] J. J. Crassous, R. Régisser, M. Ballauff, and N. Willenbacher, "Characterization of the viscoelastic behavior of complex fluids using the piezoelastic axial vibrator," *Journal of Rheology*, vol. 49, no. 4, pp. 851–863, 2005.

[84] T. M. Squires and T. G. Mason, "Fluid mechanics of microrheology," *Annual review of fluid mechanics*, vol. 42, 2010.

[85] T. Mason, K. Ganesan, J. Van Zanten, D. Wirtz, and S. Kuo, "Particle tracking microrheology of complex fluids," *Physical Review Letters*, vol. 79, no. 17, p. 3282, 1997.

[86] G. Fritz, W. Pechhold, N. Willenbacher, and N. J. Wagner, "Characterizing complex fluids with high frequency rheology using torsional resonators at multiple frequencies," *Journal of Rheology*, vol. 47, no. 2, pp. 303–319, 2003.

[87] K. B. Arbogast, K. L. Thibault, B. S. Pinheiro, K. I. Winey, and S. S. Margulies, "A high-frequency shear device for testing soft biological tissues," *Journal of biomechanics*, vol. 30, no. 7, pp. 757–759, 1997.

[88] N. Willenbacher and C. Oelschlaeger, "Dynamics and structure of complex fluids from high frequency mechanical and optical rheometry," *Current Opinion in Colloid & Interface Science*, vol. 12, no. 1, pp. 43–49, 2007.

[89] T. G. Mason and D. Weitz, "Optical measurements of frequency-dependent linear viscoelastic moduli of complex fluids," *Physical review letters*, vol. 74, no. 7, p. 1250, 1995.

[90] B. J. Berne and R. Pecora, *Dynamic light scattering: with applications to chemistry, biology, and physics*. Courier Corporation, 2000.

[91] D. P. Cattin, "Image restoration: Introduction to signal and image processing," *MIAC, University of Basel. Retrieved*, vol. 11, p. 93, 2013.

[92] L. MacDonald, *Digital Heritage*. Routledge, 2006.

[93] B. Qian, J. Park, and K. S. Breuer, "Large apparent slip at a moving contact line," *Physics of Fluids*, vol. 27, no. 9, p. 091703, 2015.

[94] T. Schmidt, G. Schütz, W. Baumgartner, H. Gruber, and H. Schindler, "Imaging of single molecule diffusion," *Proceedings of the National Academy of Sciences*, vol. 93, no. 7, pp. 2926–2929, 1996.

[95] E. Afik, "Robust and highly performant ring detection algorithm for 3d particle tracking using 2d microscope imaging," *Scientific reports*, vol. 5, p. 13584, 2015.

[96] B. Zhang and J. P. Allebach, "Adaptive bilateral filter for sharpness enhancement and noise removal," *IEEE transactions on Image Processing*, vol. 17, no. 5, pp. 664–678, 2008.

[97] W. Jiang, M. L. Baker, Q. Wu, C. Bajaj, and W. Chiu, "Applications of a bilateral denoising filter in biological electron microscopy," *Journal of structural biology*, vol. 144, no. 1-2, pp. 114–122, 2003.

[98] T. G. Mason, "Estimating the viscoelastic moduli of complex fluids using the generalized stokes–einstein equation," *Rheologica Acta*, vol. 39, no. 4, pp. 371–378, 2000.

[99] E. R. Weeks, J. C. Crocker, A. C. Levitt, A. Schofield, and D. A. Weitz, "Three-dimensional direct imaging of structural relaxation near the colloidal glass transition," *Science*, vol. 287, no. 5453, pp. 627–631, 2000.

[100] T. Toyota, D. A. Head, C. F. Schmidt, and D. Mizuno, "Non-gaussian athermal fluctuations in active gels," *Soft Matter*, vol. 7, no. 7, pp. 3234–3239, 2011.

[101] X.-L. Wu and A. Libchaber, "Particle diffusion in a quasi-two-dimensional bacterial bath," *Physical review letters*, vol. 84, no. 13, p. 3017, 2000.

[102] A. Einstein, *Investigations on the Theory of the Brownian Movement*. Courier Corporation, 1956.

[103] J. Desbrieres, M. Hirrien, and S. Ross-Murphy, "Thermogelation of methylcellulose: rheological considerations," *Polymer*, vol. 41, no. 7, pp. 2451–2461, 2000.

[104] L. J. Fauci and A. McDonald, "Sperm motility in the presence of boundaries," *Bulletin of mathematical biology*, vol. 57, no. 5, pp. 679–699, 1995.

[105] M. J. Mack, "Minimally invasive and robotic surgery," *Jama*, vol. 285, no. 5, pp. 568–572, 2001.

[106] I. Kassim, L. Phee, W. S. Ng, F. Gong, P. Dario, and C. A. Mosse, "Locomotion techniques for robotic colonoscopy," *IEEE Engineering in Medicine and Biology Magazine*, vol. 25, no. 3, pp. 49–56, 2006.

[107] J. J. Abbott, Z. Nagy, F. Beyeler, and B. J. Nelson, "Robotics in the small, part i: microbotics," *IEEE Robotics & Automation Magazine*, vol. 14, no. 2, pp. 92–103, 2007.

[108] B. J. Nelson, I. K. Kaliakatsos, and J. J. Abbott, "Microrobots for minimally invasive medicine," *Annual review of biomedical engineering*, vol. 12, pp. 55–85, 2010.

[109] M. C. Marchetti, J.-F. Joanny, S. Ramaswamy, T. B. Liverpool, J. Prost, M. Rao, and R. A. Simha, "Hydrodynamics of soft active matter," *Reviews of Modern Physics*, vol. 85, no. 3, p. 1143, 2013.

[110] S. Suarez and A. Pacey, "Sperm transport in the female reproductive tract," *Human reproduction update*, vol. 12, no. 1, pp. 23–37, 2006.

[111] S. G. Taylor, "The dynamics of thin sheets of fluid," 1959.

[112] J. Oldroyd, "On the formulation of rheological equations of state," *Proc. R. Soc. Lond. A*, vol. 200, no. 1063, pp. 523–541, 1950.

[113] E. E. Riley and E. Lauga, "Small-amplitude swimmers can self-propel faster in viscoelastic fluids," *Journal of theoretical biology*, vol. 382, pp. 345–355, 2015.

[114] T. D. Montenegro-Johnson, D. J. Smith, and D. Loghin, "Physics of rheologically enhanced propulsion: different strokes in generalized stokes," *Physics of Fluids*, vol. 25, no. 8, p. 081903, 2013.

[115] C. Datt, L. Zhu, G. J. Elfring, and O. S. Pak, "Squirming through shear-thinning fluids," *Journal of Fluid Mechanics*, vol. 784, 2015.

[116] Y. Hyon, T. R. Powers, R. Stocker, H. C. Fu, *et al.*, "The wiggling trajectories of bacteria," *Journal of Fluid Mechanics*, vol. 705, pp. 58–76, 2012.

[117] X. Shen and P. E. Arratia, "Undulatory swimming in viscoelastic fluids," *Physical review letters*, vol. 106, no. 20, p. 208101, 2011.

[118] S. Gómez, F. A. Godínez, E. Lauga, and R. Zenit, "Helical propulsion in shear-thinning fluids," *Journal of Fluid Mechanics*, vol. 812, 2017.

[119] J. M. Katona, S. D. Njaradi, V. J. Sovilj, L. B. Petrović, B. B. Marčeta, and J. L. Milanović, "Rheological properties of hydroxypropylmethyl cellulose/-sodium dodecylsulfate mixtures," *Journal of the Serbian Chemical Society*, vol. 79, no. 4, p. 457, 2013.

[120] T. Gillespie, "The viscosity of concentrated polymer solutions," *Journal of Polymer Science Part A: Polymer Chemistry*, vol. 46, no. 148, pp. 383–393, 1960.

[121] M. A. Constantino, M. Jabbarzadeh, H. C. Fu, and R. Bansil, "Helical and rod-shaped bacteria swim in helical trajectories with little additional propulsion from helical shape," *Science advances*, vol. 2, no. 11, p. e1601661, 2016.

[122] Y. Zhang, G. Li, and A. M. Ardekani, "Reduced viscosity for flagella moving in a solution of long polymer chains," *Physical Review Fluids*, vol. 3, no. 2, p. 023101, 2018.

[123] Y. Man, W. Page, R. J. Poole, and E. Lauga, "Bundling of elastic filaments induced by hydrodynamic interactions," *Physical Review Fluids*, vol. 2, no. 12, p. 123101, 2017.

[124] L. Landau and E. Lifshitz, "Theory of elasticity, 3rd," *ed: Pergamon Press, Oxford, UK*, 1986.

[125] O. S. Pak, E. Lauga, C. Duprat, and H. Stone, "Theoretical models of low-reynolds-number locomotion," *Fluid–structure interactions in low-Reynolds-number flows*, pp. 100–167, 2015.

[126] R. Dreyfus, J. Baudry, M. L. Roper, M. Fermigier, H. A. Stone, and J. Bibette, "Microscopic artificial swimmers," *Nature*, vol. 437, no. 7060, p. 862, 2005.